Electron cloud buildup simulations for the LHC

Project-Proposal von Philipp Dijkstal
Tag der Einreichung:

1. Gutachten: Prof. Dr. rer. nat. Oliver Boine-Frankenheim
2. Gutachten: Dr. rer. nat. Giovanni Iadarola

TECHNISCHE
UNIVERSITÄT
DARMSTADT

Fachbereich Physik
Theorie Elektro-
magnetischer Felder (TEMF)

Electron cloud buildup simulations for the LHC

Vorgelegtes Project-Proposal von Philipp Dijkstal

1. Gutachten: Prof. Dr. rer. nat. Oliver Boine-Frankenheim
2. Gutachten: Dr. rer. nat. Giovanni Iadarola

Tag der Einreichung:

Abstract

Electron clouds are a phenomenon that arises in accelerators operating with positively charged particles. They are the result of an interaction between the beam and the confining chamber. Primary electrons, that can by generated by various processes, are accelerated by the beam and impinge on the chamber walls, which in turn emits secondary electrons (secondary electron emission). This process can trigger an avalanche multiplication of the electrons and the formation of an electron cloud. The impacting electrons deposit energy on the chamber's wall which can become a significant heat load especially in cryogenic environments, as it is the case for a major part of the Large Hadron Collider (LHC) at CERN. The consequences of this effect are very important for the LHC and future accelerators including the LHC luminosity upgrade (HL-LHC). The main goal of this work is to improve the understanding of the electron cloud induced heat loads, from the side of simulations and measurements. This report describes the steps that have been made so far and their implications.

The heat load data analysis has been improved by recalculating and storing the heat loads measured in different cryogenic sectors of the LHC for all proton fills in 2015 and 2016. An excerpt of this data has been created, which includes also various kinds of beam parameters. Its analysis proved to be very useful in identifying features and patterns of the electron cloud induced heat loads that went previously unnoticed, and that could be relevant for future studies.

Information has been collected also in dedicated tests performed at the LHC during Machine Development sessions. Three fills have been performed in 2016 with the purpose of exploring the intensity dependence of electron cloud effects in the regime of bunch intensities between 0.6 and $1.1{\cdot}10^{11}$ particles per bunch. Their analysis revealed a sensitivity of the heat load on the bunch intensity that should be reproducible by electron cloud buildup simulations. This is a necessary pre-condition to use these simulations in order to make predictions for intensity ranges that are relevant for the HL-LHC upgrade but that are unavailable for the current LHC accelerator.

In the future work leading up to the Master's thesis, emphasis will be laid on improving the electron cloud buildup simulations for the LHC, using the available measurements to identify possible weaknesses. In the course of this it will also be necessary to improve the model of the LHC cryogenic cell, including for example higher order magnets (sextupoles, octupoles) that have so far been neglected in electron cloud studies at CERN. The generation of photoelectrons through synchrotron radiation, that act as primary electrons for the buildup-process will also be examined in detail.

Contents

1 Introduction

This chapter introduces the Large Hadron Collider (LHC), the accelerator which is subject to the studies of this report. To help readers unfamiliar with the jargon used at CERN, basic aspects of beam operations are introduced. Later on, the need for further electron cloud studies at the LHC is motivated with necessary predictions on electron cloud effects for future machines and available data from the previous two years of beam operations at the LHC.

1.1 Large Hadron Collider

The Large Hadron Collider is the world's largest particle accelerator and capable of accelerating protons and lead ions. These beams are collided in four main experiments to investigate fundamental laws of physics. The detectors at the interaction points are ATLAS and CMS, that have most notably found the Higgs Boson in 2012 [1], ALICE which specialises on heavy ion collisions and LHCb, designed to study particles that contain bottom quarks. The LHC is supplied with protons by the injector complex made by Linac 2, the PS Booster, the Proton Synchrotron (PS) and the Super Proton-Synchrotron (SPS) (see Fig. 1.1). If ions are accelerated instead, an alternative route is being taken where Linac 2 and the Booster are replaced by Linac 3 and the Low Energy Ion Ring (LEIR). This report is however focused on proton operations.

The long-term operational schedule of the LHC is divided into runs and long shutdowns (LS), each of which lasts between two and four consecutive years [2]. The beam operations take place during the runs, while the LS are reserved for maintenance and upgrades in the LHC and its injector complex. Figure 1.2 shows the time plan for the following years, and includes also the high luminosity upgrade of the LHC.

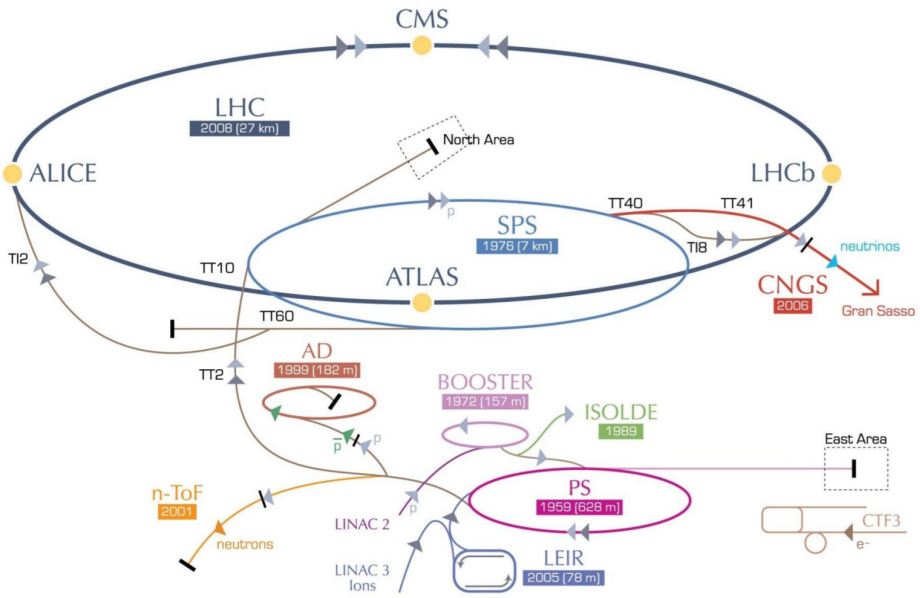

Figure 1.1: The accelerator complex at CERN including some signature experiments and detectors [3].

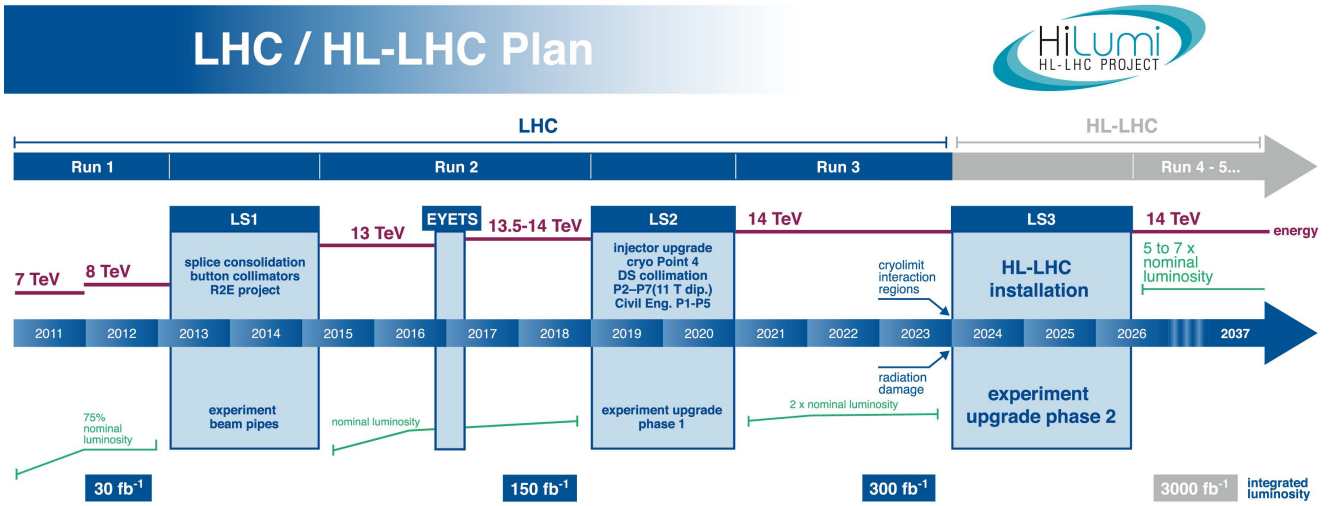

Figure 1.2: The schedule of the LHC operations since 2011, including the planned high luminosity upgrade. Some abbreviations used in this figure are Long Shutdown (LS) and Extended Year-End Technical Stop (EYETS). At the bottom, the expectations on the beam luminosity are noted in fb^{-1}. This is are a measure for the number of collisions in the detectors and therefore also the performance of the LHC from the point of view of the physics experiments. The collision energy in red is the sum of the energies of both beams [4].

1.2 A typical fill for proton physics at the LHC

This section explains the main phases of a typical fill for proton physics, where beams are put into collision for the LHC experiments. An overview is provided in Fig. 1.3, where the energy, the total intensities, the bunch length and the average heat load on the cryogenic cells for each arc are shown.

Such a fill begins right after the previous beam has left the accelerator, meaning that the superconducting magnets have to be ramped down first. Multiple injections from the SPS are necessary to refill the LHC because of its larger circumference. Shortly after the injection of the last train, the machine is ready to ramp the beam energy from injection (450 GeV) to flat top energy (6.5 TeV). The beam size at the interaction regions in the LHC is decreased (squeezed) to increase the collision rate (luminosity). The machine parameters are adjusted to optimize the performance, before the "stable beams" condition is declared and the experiments begin the collection of data. The intensity starts to decrease notably afterwards, mainly because the collided protons are lost. This is also called the luminosity burn-off. Furthermore the energy spread of the beam shrinks as the protons with higher energy emit more synchrotron radiation. Because bunch length and energy spread are linked through the synchrotron motion, the former also decreases in the process (see Fig. 1.3). The machine is meant to operate for several hours in this way, until the intensity becomes too low and a planned dump takes place. Often enough however, the beam has to be dumped early for machine safety reasons. Because of this, there is a wide spread in the duration of proton physics fills, ranging from only several hours to 40 hours.

A quick overview of the basic beam properties relevant for electron clouds is provided here. Most fills for proton physics in 2016 contained between 2040 and 2220 bunches, with up to $1.3{\cdot}10^{11}$ protons per bunch (see also Fig. 4.1). A bunch spacing of 25 ns has been the main operational mode since 2015. The filling pattern is formed by the LHC injector complex, especially the PS and the SPS, and is occasionally changed to optimize the machine performance. It consists of batches of consecutively filled bunch slots separated by empty slots, see Fig. 1.4. The batches are separated by gaps of 225 ns, corresponding to the rise time of the SPS injection kicker. Several batches form a train, and consecutive trains are interrupted by 925 ns of empty slots due to the LHC injection kicker rise time. An abort gap of 3 μs has to be present at one point in the filling pattern, to enable an extraction at high energy towards the beam dump [5].

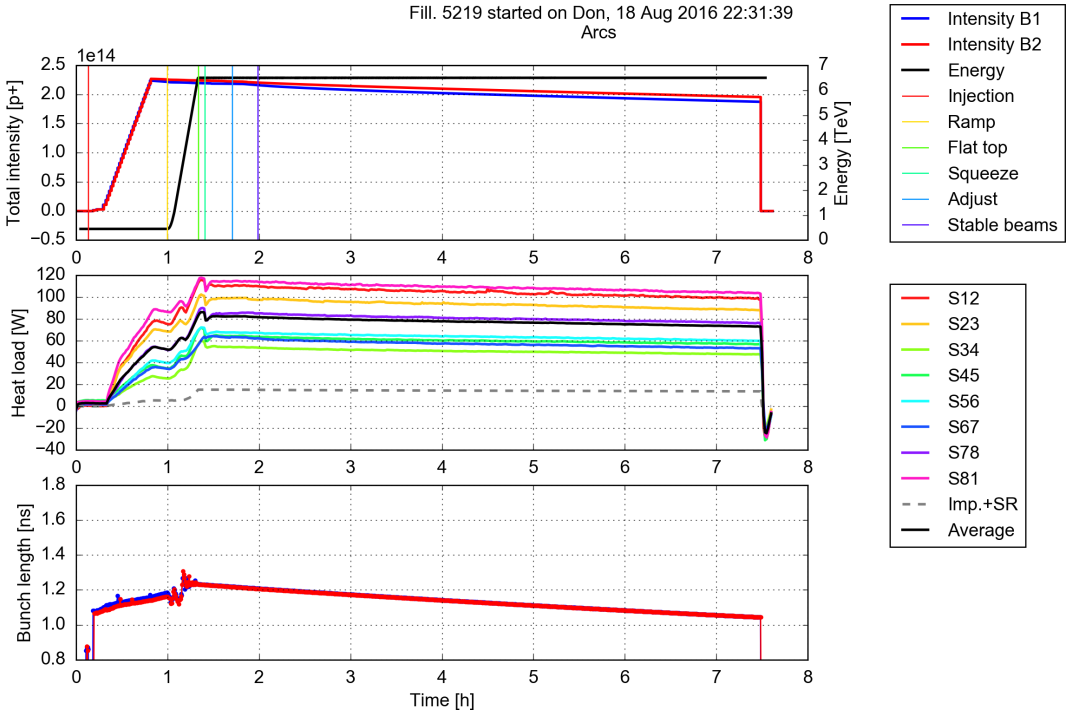

Figure 1.3: In the upper plot, the energy and the total beam intensities are shown during a typical fill in the LHC. It is also indicated when the status of the fill changes. The middle plot features the average heat loads on the cells of the cryogenic system in the eight arcs of the LHC. The sources of heat load besides the electron cloud are impedance and synchrotron radiation. At the bottom, the average bunch length is shown.

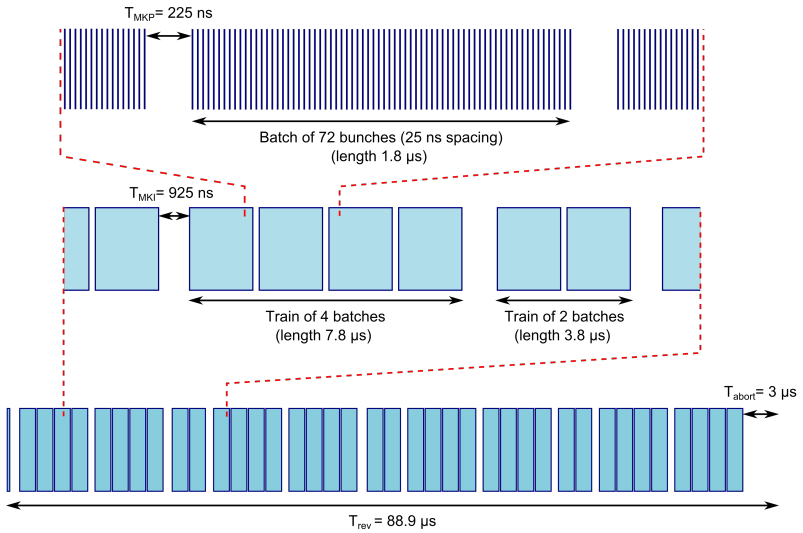

Figure 1.4: The LHC filling pattern consists of several trains, these in turn consist of several batches of consecutively filled bunch slots. The filling pattern has a great influence on the electron cloud effects [5].

The number of electrons in a beam pipe can grow large enough to become significant mainly because of secondary electron emission. It means that, depending on properties of the surface, one impinging electron can cause multiple other electrons to emerge into the chamber as well. It requires the presence of primary electrons, which can for example be created by the photoelectric effect or residual gas ionization. This can lead to a substantial increase of electrons in the chamber, called electron cloud (EC). This process eventually reaches an equilibrium state when the space charge effect of the already present electrons prevents a further increase. The cloud of electrons interacts with the beam through electro-magnetic forces and can distort the beam quality. Another problem is that in environments such as the LHC with its large number of magnets at cryogenic temperatures, the heat that the many electrons cause while impinging on walls has to be absorbed by the cooling system at very low temperatures. If these heat loads were to reach the limits of the cooling system, the beam parameters would have to be modified to allow for a continuation of beam operations. Already for the current LHC, the cryoplants for some of the arcs operate at around 75% of their maximum cooling capacity. This is shown in Fig. 1.3 where heat loads of up to 120 W per cryogenic cell are measured as the average for some arcs, while the performance limit of the cooling circuits is known to be 160 W per cryogenic cell.

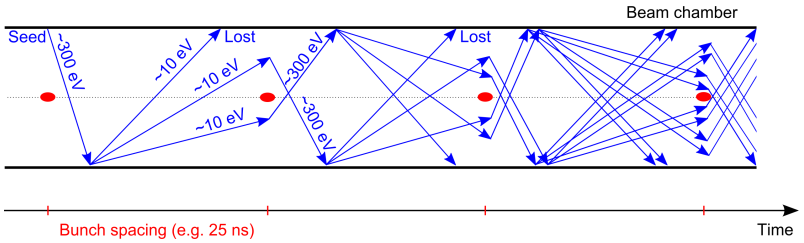

Figure 1.5: This sketch visualizes how electrons can trigger an avalanche effect as they are accelerated by the positively charged beam and then hit the wall, causing more electrons to enter the chamber. In the end, the population is dense enough to be called a cloud of electrons [5].

Electron cloud effects have been studied at CERN for many years. The CERN electron cloud team performs simulations and experimental work to improve the operation of the LHC and future machines. These include most importantly the planned HL-LHC and the proposed Future Circular Collider (FCC). For each of these accelerators, EC effects have been recognized as among the major performance limitations [4, 6]. A good understanding of these effects is therefore crucial for the future of high energy hadron accelerators. The upgrade to HL-LHC will require higher bunch intensities of planned $2.2 \cdot 10^{11}$ protons per bunch [4], while the current LHC has only operated with up to $1.3 \cdot 10^{11}$ in run 2. The cooling system will not be upgraded.

In contrast to previous studies that include buildup simulations for LHC [5], the data that has been accumulated during run 2 is now available. Especially the measured heat loads on the cryogenic system can provide insight, as they are primarily caused by electron clouds. This is even more significant because EC effects are much stronger at a bunch spacing of 25 ns, the default configuration of run 2 that is also going to be used for the HL-LHC. During the preceding run 1, 50 ns were used for the most part instead.

This leaves several frontiers for this work. On one side, the LHC cryogenic cells, where the heat loads are measured, have to be simulated using the best knowledge available. On the other side, the measured heat loads themselves need to be closely examined to ensure that they are correctly interpreted. Furthermore, the large set of especially heat load data should be analyzed to find previously unknown features and scaling laws of electron cloud effects.

2 Electron cloud simulations

This chapter starts with a brief description of the secondary emission model used for the simulation software PyECLOUD. This tool has been used at CERN for several years, and its fundamental aspects are recapped. Examples of buildup simulations for quadrupoles and dipoles are shown. Afterwards, several parameters from the previously mentioned SEY model have been varied to show the impact on the heat loads yielded by the simulations.

2.1 Secondary emission of electrons

The process of secondary electron emission (SEY) is subject of ongoing research at CERN and other labs. The CERN electron cloud team uses a model based on experimental data for copper [5, 7, 8, 9, 10, 11]. The secondary emission parameter $\delta(E)$ is defined as the ratio between the electron current onto the wall and the emitted current. It is dependent on the energy of the impinging electrons and their angle of incidence θ.

$$\delta(E,\theta) = \frac{I_{\text{Emit}}}{I_{\text{imp}}(E,\theta)} \tag{2.1}$$

The emitted current, and therefore also $\delta(E)$, can be divided into parts formed by true secondary electrons and elastically scattered electrons. The latter are modelled in the following way, not depending on θ:

$$\delta_{\text{elas}}(E) = R_0 \left(\frac{\sqrt{E} - \sqrt{E+E_0}}{\sqrt{E} + \sqrt{E+E_0}} \right)^2 \tag{2.2}$$

For the two parameters R_0 and E_0, 0.7 and 150 eV are used by default for the LHC beam chamber. However there are conflicting opinions on the shape of the for the very low energy part of this relation, where some say $\delta_{\text{elas}}(E=0)$ should approach 0 or 1. The value 0.7 for R_0 is a compromise following this disagreement [12, 13].

The true secondary emission yield depends on the shape parameter s and on E_{max}, the incident energy resulting to the most secondary electrons.

$$\delta_{\text{true}}(E,\theta) = \delta'_{\text{max}}(\theta) \frac{s \frac{E}{E'_{\text{max}}(\theta)}}{s - 1 + \left(\frac{E}{E'_{\text{max}}(\theta)} \right)^s} \tag{2.3}$$

$$\delta'_{\text{max}}(\theta) = \delta_{\text{max}}\, e^{\frac{1-\cos\theta}{2}} \tag{2.4}$$

$$E'_{\text{max}}(\theta) = E_{\text{max}} (0.3 + 0.7\cos\theta) \tag{2.5}$$

The angular dependence is motivated by the increased time that electrons spend close to the surface in case they have a larger angle of incidence. Therefore their chance to produce secondaries is enhanced. Plots that show δ_{true} and δ_{elas} are found in Fig. 2.1. It becomes clear that the elastic scattering only happens for low incident energies, and that high angles of incidence significantly increase the emission of true secondaries. Because δ_{max} is expected to change in the process of electron cloud mitigated scrubbing (see Sec. 4.2), it is scanned in almost all simulation studies and often called "the SEY parameter". E_{max} and s on the other hand have been fixed at 1.35 and 330 eV for most simulations.

The energy of the emitted secondaries follows a log-normal distribution specified by μ and σ, normally determined as 1.0828 and 1.6636 (see [5] and references therein).

$$\frac{\mathrm{d}n_{\text{true}}}{\mathrm{d}E} = \frac{1}{E\sigma\sqrt{2\pi}} e^{-\frac{(ln(E)-\mu)^2}{2\sigma^2}} \tag{2.6}$$

The angle of emitted secondaries follows a cosine distribution.

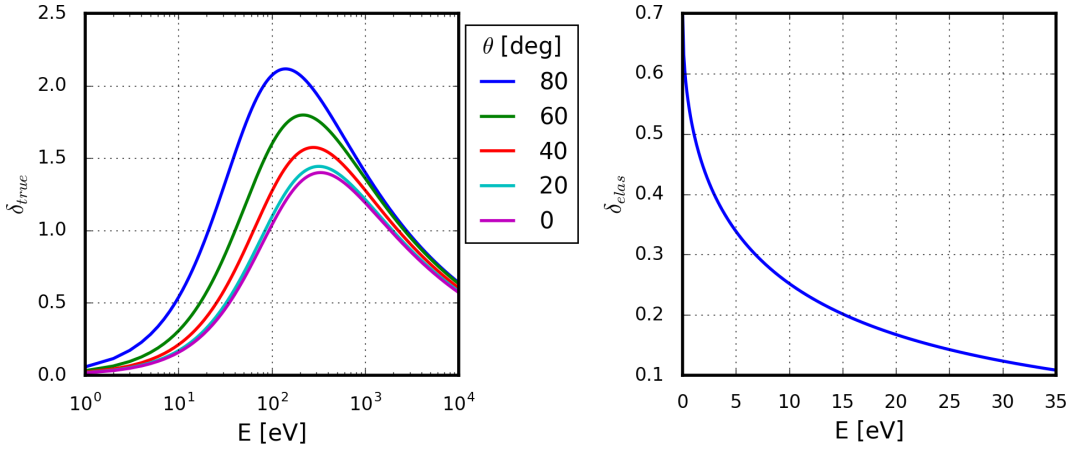

Figure 2.1: These curves correspond to Eq. (2.3) and (2.2), and show the ratios of true secondary and elastically scattered electron currents with respect to the impinging current.

2.2 PyECLOUD buildup simulations

PyECLOUD is a 2D code that simulates the EC buildup in a thin slice around a certain section of a particle accelerator. Electrons are grouped in macro-particles (MP), in order to achieve a reasonable computational burden. The program is thoroughly described in [5], a summary of the principal features is provided here. Figure 2.3 shows a flowchart of the main loop in the simulation.

1. It begins with the seeding process, where gasionization and photoemission by synchrotron radiation are implemented. Alternatively, an initial distribution of primary electrons can be specified, without considering a seeding mechanism. This is a valid approximation in case there is multipacting and the seeding process would soon become irrelevant anyways compared to the large number of secondaries.
2. The beam is approximated to be rigid, meaning it remains unaffected by the EC for the duration of the simulation. The electromagnetic fields of the beam have therefore to be calculated only once in the initialization stage. The beam charge distribution takes the following form

$$\rho(x,y,s,t) = \lambda(s-ct)\rho_{\perp}(x,y), \tag{2.7}$$

   where the transverse beam profile $\rho_{\perp}$ is assumed to be Gaussian. The longitudinal profile λ is either specified or also generated with a Gaussian form.
3. A Particle in Cell (PIC) algorithm is used to obtain the space charge forces of the electron cloud. This means that the macro-particles are projected on a grid, and the electrostatic potential is calculated with the Finite Differences method. The electric field is the first derivative of the electrostatic potential.
4. The MPs are tracked in the chamber while they are exposed to the electromagnetic forces from the confining magnet, the beam and the electrons themselves. The Lorentz force determines the movement of the particles.

$$\mathbf{F} = -q\,(\mathbf{E} + \mathbf{v} \times \mathbf{B}) \tag{2.8}$$

5. When macro-particles impact on the chamber walls, it is decided how many of them are treated as elastically reflected or as a secondary electrons. In case of the latter, the size of the MP may grow. A dedicated procedure to split up MPs that are too large, and to remove MPs that are very small is implemented. The number of macro-particles is therefore dynamic.

For the beam chamber as installed at the LHC Arcs, one train of protons has been simulated in dipoles and quadrupoles, see Fig. 2.2. The magnetic fields and beam parameters are those that occur at 6.5 TeV during a typical fill. The 4 σ bunch length was set to 1.2 ns, and the bunch intensity to 1.1 $\cdot 10^{11}$ particles per bunch. The train consisted of 4 batches of 72 bunches each, separated by 8 empty slots. The parameter $\delta_{\max}$ has been scanned, while the others are set as described in the previous section. A uniform initial distribution of 10^7 electrons per m has been in the chamber.

It is possible to use a measured beam profile as an input, where the bunch lengths and bunch intensities from the FBCT (Fast Beam Current Transformer) for all bunches are used to create a Gaussian shaped beam. Whenever an MP hits the chamber wall, the deposited energy is calculated and saved. The sum of these impacts yields the simulated heat load, which can in turn be compared with the measured heat loads from the same beam (see Fig. 2.4).

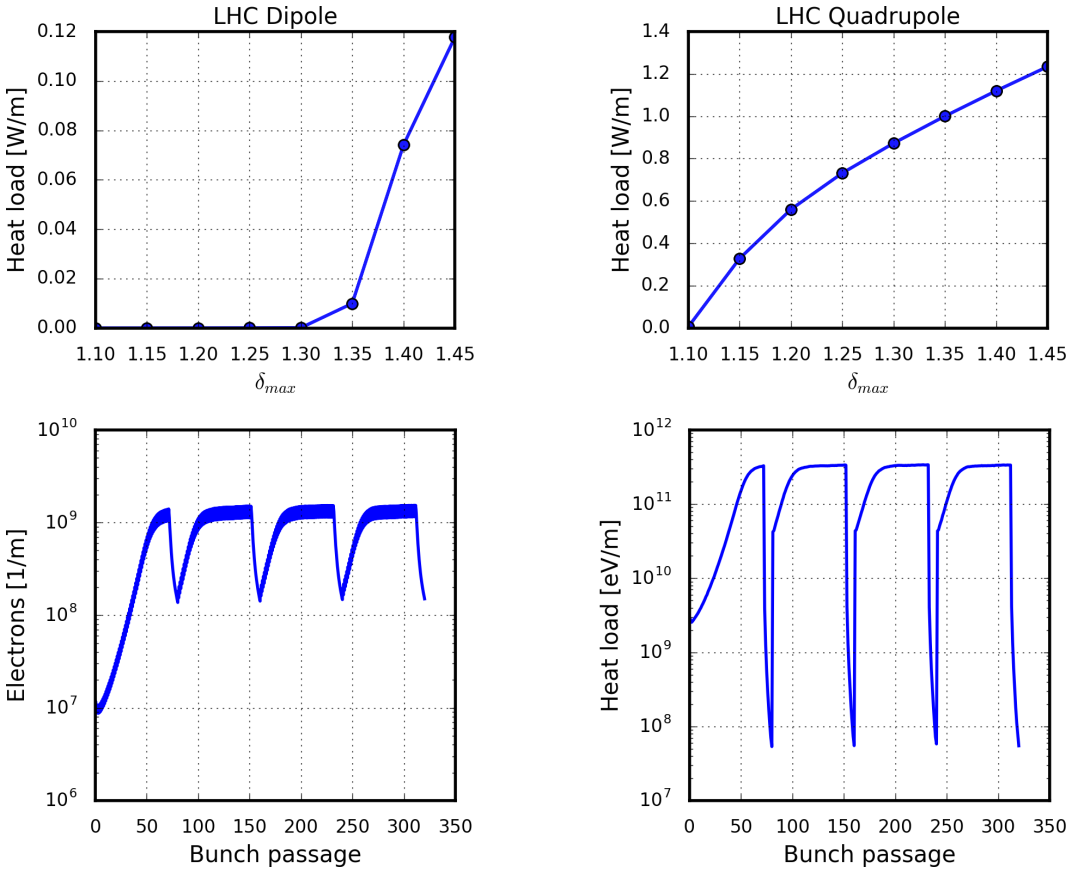

Figure 2.2: One train of protons (288 bunches) has been simulated under variation of $\delta_{\max}$. The upper plots show the resulting heat loads for dipoles and quadrupoles. The bottom plot features the number of electrons and the heat loads per bunch passage. These are taken from the simulation for dipoles with $\delta_{\max} = 1.45$.

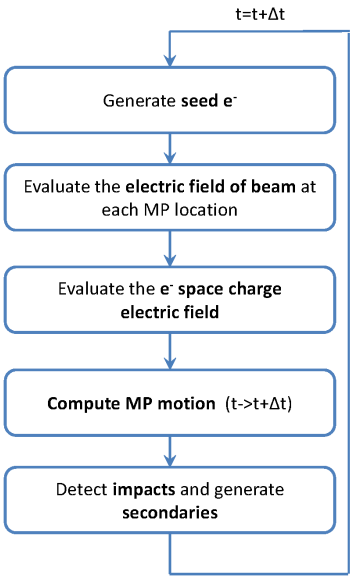

Figure 2.3: A flowchart of the PyECLOUD main loop [5].

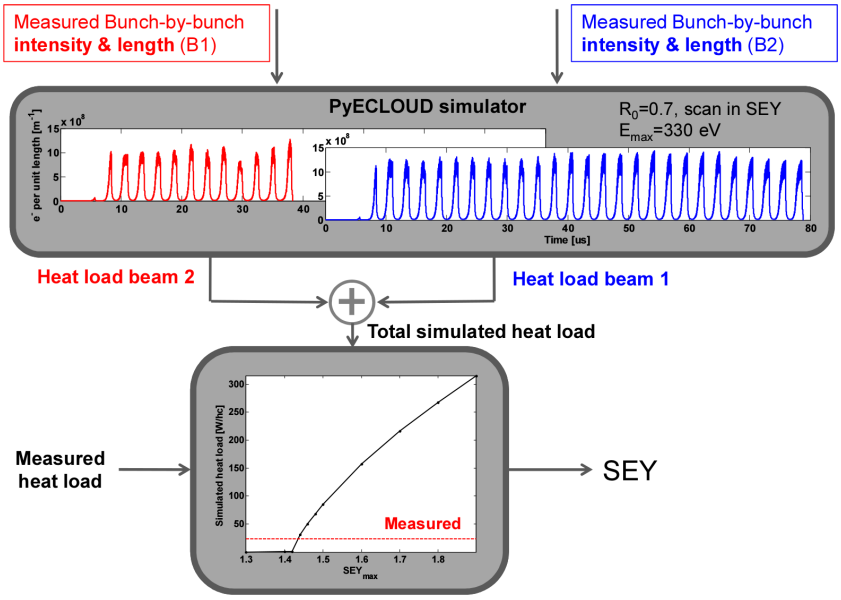

Figure 2.4: This sketch demonstrates how PyECLOUD can be utilized to infer the $\delta_{\max}$ (SEY) parameter in the LHC. This implies that the other parameters, for example R_0 and $E_{\max}$, are known [5].

Some of the input parameters for the SEY model have been varied in order to find out how sensitive the simulated heat loads are. All other parameters have been identical to the simulations shown in Fig. 2.2.

Figure 2.5 (top) shows the changes in heat loads when E_{max} from Eq. (2.3) is altered. It has opposite effects on dipoles and quadrupoles. This can be explained by trapped electrons in the quadrupoles, where the increasing fields in transverse direction can have the effect of an magnetic bottle. These electrons can be accelerated by multiple bunch passages and reach higher energies before impacting the wall. In case of the dipole, there are no possible trapping effects, and the occurring energies are lower.

Below in Fig. 2.5, the enhancement of the secondary emission with respect to the angle of incidence has been varied. The factor corresponds to A in the following equation, which replaces $\frac{1}{2}$ in Eq. (2.4):

$$\delta'_{\mathrm{max}}(\theta) = \delta_{\mathrm{max}}\, e^{A\cdot(1-\cos\theta)} \tag{2.9}$$

When the enhancement is fully removed (red curve), the EC effects for the quadrupole are diminished by a large factor. This means that most impinging electrons in this device do so with large angles of incidence, which is not the case for dipoles.

In Fig. 2.6, the energy distribution of secondary electrons has been changed (see Eq. (2.6)). First, only μ has been varied, which changes the SEY threshold for the dipoles, but not to a great extent for the quadrupoles. The second part changed both μ and σ by the specified factors, while the original curve is retained in red. This barely shifts the thresholds for both devices, but has a greater effect overall on the quadrupoles.

Parameters that have not been scanned so far include R_0 and E_0 for the elastically scattered SEY, and the angular dependence of the secondary electrons.

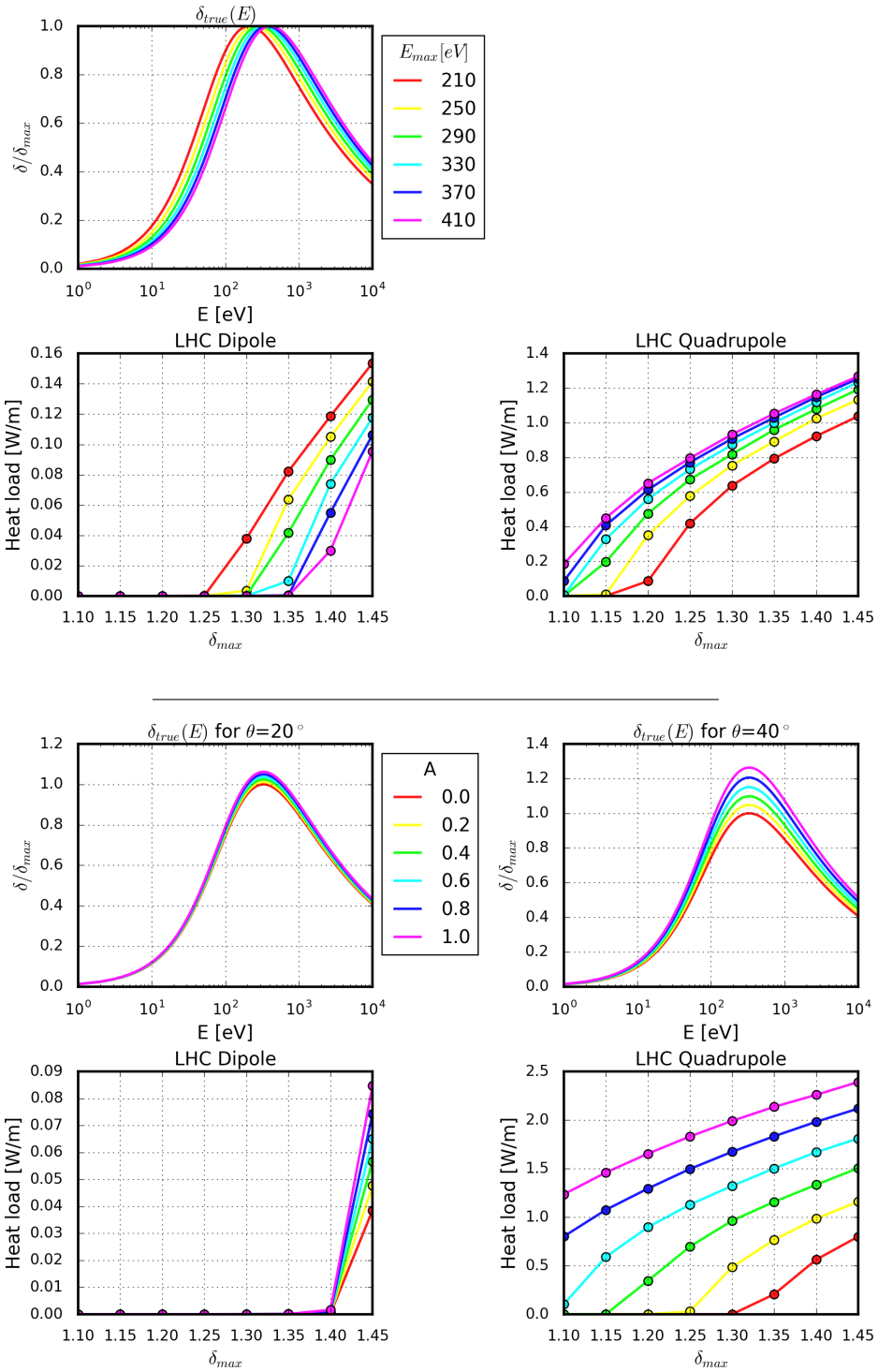

Figure 2.5: Top: the $E_{\max}$ parameter defines the secondary emission yield and has been varied for this set of simulations. With increasing $E_{\max}$, the EC in the dipoles decreases while it increases in the quadrupoles. Bottom: the factor A enhances or diminishes the increase of SEY with the angle electrons impinge on the walls, see Eq. (3.5). Normally is is defined as 0.5. The top two plots show the secondary emission yield for angles of 20° and 40°. This has a much larger effect on the quadrupoles.

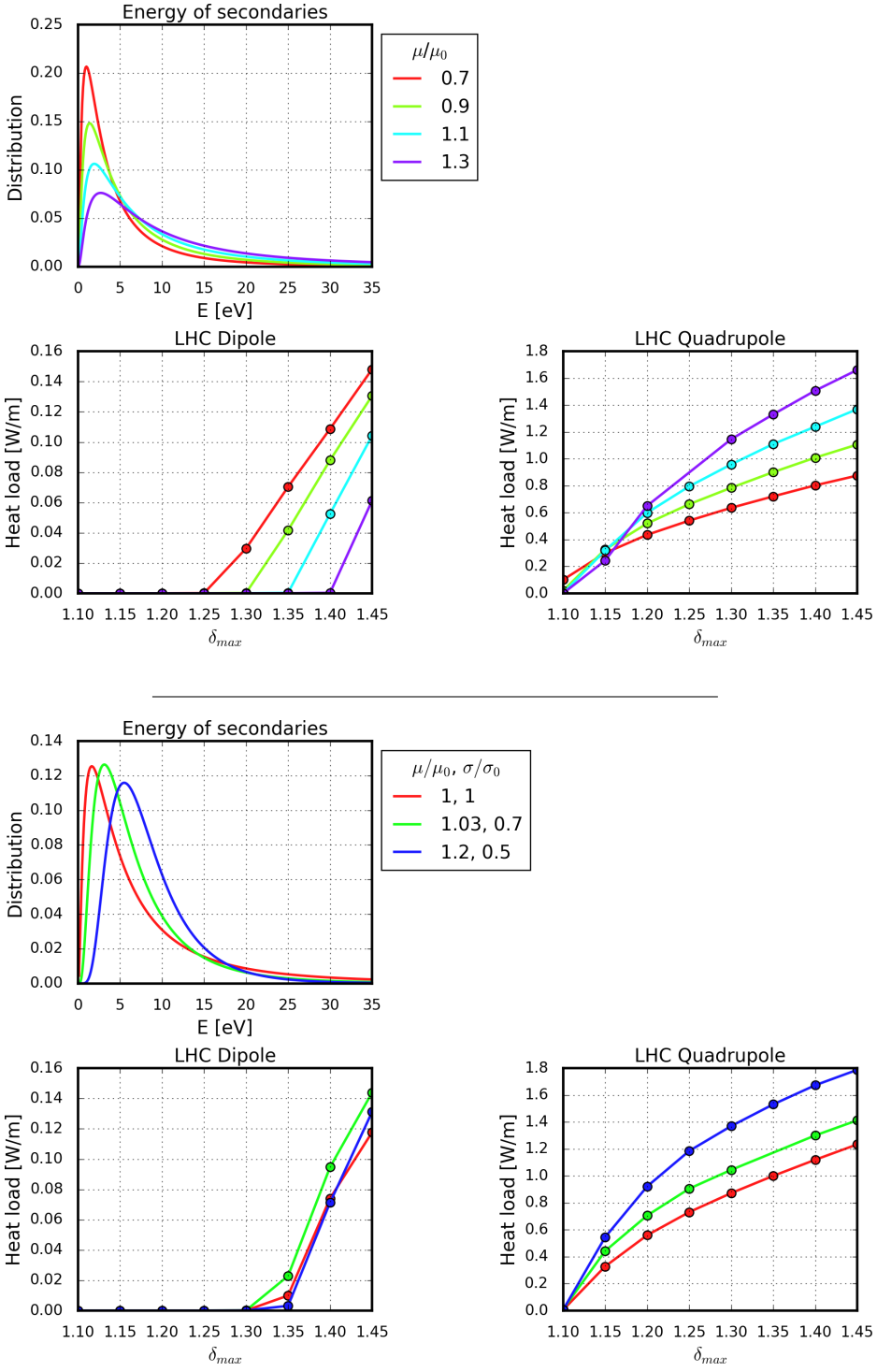

Figure 2.6: The energy distribution of secondary electrons has been modified. The upper part shows the effect of changing μ in the underlying log-normal distribution. For the lower part, both μ and σ have been changed.

3 Heat load measurements and LHC cooling system

An important part of this work is to closely examine the heat loads that are being caused by electron cloud. These are measured at the LHC and enhance our knowledge of EC effects. Furthermore they can be compared to simulation results.

This chapter describes the parts of the LHC cryogenic system that are relevant for this work, and how the beam screen cooling power is being measured. It is also necessary to estimate the components of the heat load that are not related to electron cloud and subtract them.

For the arc cells, only the combined heat load from multiple magnets and magnet types as well as their interconnections is being measured. It is therefore not easy to disentangle their contributions which are expected to by very different. Because of this, there are currently three specially instrumented cells with temperature sensors after each magnet. The detailed analysis of these cells, only partially attempted before, is part of this work.

For reasons that are outlined later in this chapter, it has been necessary to reimplement the heat load calculation as a more flexible module than what has been used prior to this work[1]. One section is devoted to a validation of the results, where also parts of work done by other people is shown to provide the reader with the necessary overview.

3.1 Cryogenics

Outside of the crossing regions of the LHC, the two particle beams are enclosed by separate vacuum chambers (beam tubes). The superconducting magnet coils are in thermal contact to these tubes and cooled by liquid helium at 1.9 K. The part of the vacuum vessel that has this lowest temperature is also called cold mass. Figure 3.1 shows a cross-section of an arc dipole. A beam screen (BS) is installed inside the beam tubes, with the purpose of absorbing the heat load caused by the beam, see Fig. 3.2. This beam screen is thermally isolated from the cold mass and kept at a higher temperature between 4.6 and 20 K. This allows for non-isothermal cooling that is around eight times more efficient with respect to isothermal cooling at 1.9 K [14]. The BS is cooled by a flow of weakly supercritical helium through two small attached tubes.

A cryogenic cell contains three dipoles and one quadrupole, as well as the necessary correction magnets and interconnections. Because two cryogenic cells correspond to a FODO cell in terms of beam optics, these are often called half-cells. An overview of the cryogenic transfer lines for the beam screens of a cryogenic cell in the arcs is shown in Fig. 3.3. The helium in the supply header denoted C origins from the cryoplants, it supplies the cells of an arc in parallel. The pressure and temperature is measured every four cells along the header. The helium enters a cell at the location subscripted 1 in the figure. During the following transfer line towards the magnets, a sink-in heat load Q_S has to be taken into account, as the tubes rest on support posts which leads to a small thermal coupling. An electrical heater is available to stabilize the temperature and the gas flow if there are rapid changes in the required cooling power, for example at the beginning and the end of fills. The flow is split up two times afterwards, first because there are two beam screens, and then again for the two cooling tubes of each BS. The temperatures T_2 and T_3 are measured in every cell before and after the beam screens, where the amount of heat denoted Q_{BS} is transferred to the helium. The mass flow is controlled by a valve (at position 4 in Fig. 3.3), after which the helium enters the return header D. Here, the pressure and temperature T_4 and P_4 are measured once again every four cells. While the heat is absorbed, the pressure changes only by a small amount whereas the temperature increases significantly (see Fig. 3.4). The pressures P_1 and P_4, the temperatures T_1, T_2, T_3 as well as the power of the electrical heater and the valve opening are stored in the logging data base at CERN and can be conveniently accessed. The details of the heat load computation, which relies on these quantities, are shown in the following pages.

3.2 Heat load calculation

Even though the necessity of a cell by cell measurement of the heat loads has not been foreseen during the design phase of the LHC, the cryogenics team of CERN has established such a procedure, which is described in this chapter [17][2].

[1] The new module is available online under `https://github.com/pdijksta/GasFlowHLCalculator`

[2] The author is indebted to Benjamin Bradu from BE-ICS-PCS, who answered a lot of questions regarding the cryogenic system and heat load calculations. Writing the new module, that is also based on his code, would have been impossible without his help.

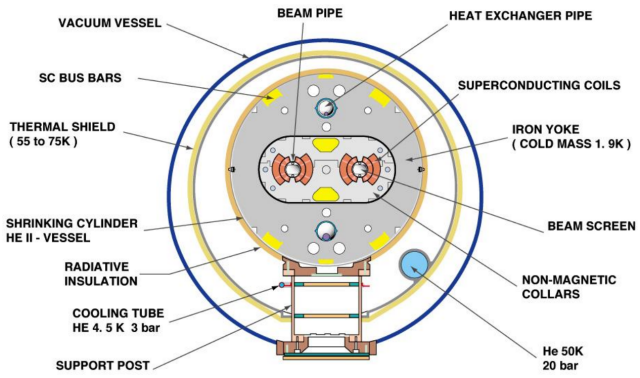

Figure 3.1: The cross section of the vacuum vessel of a dipole in the LHC [15]

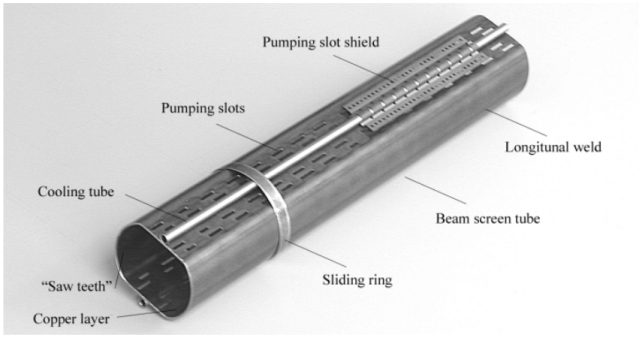

Figure 3.2: A photograph of a beam screen, which protects the cold mass at 1.9 K from beam-induced heat. Its design aperture is 44.04 mm and 34.28 mm in the horizontal and vertical planes. The purpose of the pumping slot shield is to intercept electrons [16].

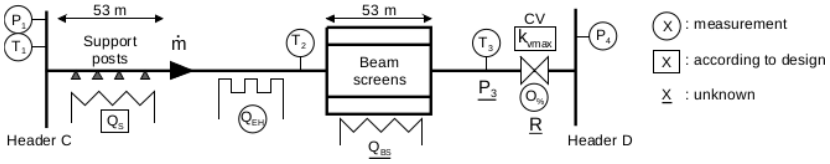

Figure 3.3: A sketch of the beam screen cooling for a typical cryogenic cell in the arcs. The different heat load contributions and the installed pressure and temperature sensors are shown [17].

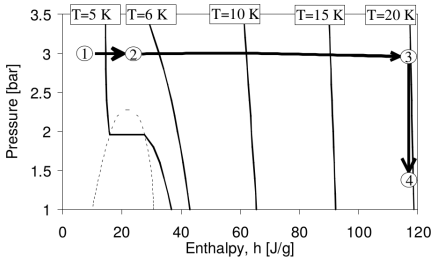

Figure 3.4: The state of the helium by design follows this line in the P-h diagram [14].

The beam induced heat load $\dot{Q}_{\mathrm{BS}}$ is obtained with an enthalpy balance. The indices of h follow Fig. 3.3 and the previously mentioned sensors.

$$\dot{Q}_{\mathrm{BS}} = \dot{m} \cdot (h_3 - h_1) - \dot{Q}_{\mathrm{EH}} - \dot{Q}_{\mathrm{S}} \tag{3.1}$$

Here, $\dot{m}$ is helium the mass flow, h the specific enthalpy and $\dot{Q}_{\mathrm{S}}$, $\dot{Q}_{\mathrm{EH}}$ are the sink-in heat load and the power of the electrical heater. The enthalpy is a function of pressure and temperature and can be obtained by interpolation of tables that have been calculated with dedicated software [18]. $\dot{Q}_S$ is part of the heat load calibration for every cell and assumed constant in time.

3.2.1 Mass flow

Because real flow meters have not been installed at the LHC, the mass flow $\dot{m}$ is instead computed through virtual flow meters. The procedure follows the Samson method [15], which is an engineering formula with empirical factors in suitable units. It requires knowledge of the thermodynamical state of the helium and the valve properties.

$$\dot{m} = 14.2 \cdot A\left(\frac{P_{\mathrm{out}}}{P_{\mathrm{in}}}\right) \cdot \sqrt{\rho_{\mathrm{in}} \cdot P_{\mathrm{in}}} \cdot K_{\mathrm{V}}(l) \tag{3.2}$$

$$K_{\mathrm{V}}(l) = K_{\mathrm{V,max}} \cdot R^{l-1} \tag{3.3}$$

$$\gamma = \frac{C_{\mathrm{p}}(P_{\mathrm{in}}, T_{\mathrm{in}}) + C_{\mathrm{p}}(P_{\mathrm{out}}, T_{\mathrm{out}})}{C_{\mathrm{v}}(P_{\mathrm{in}}, T_{\mathrm{in}}) + C_{\mathrm{v}}(P_{\mathrm{out}}, T_{\mathrm{out}})} \tag{3.4}$$

$$A\left(\frac{P_{\mathrm{out}}}{P_{\mathrm{in}}}\right) = \begin{cases} 1 & \text{if } \frac{P_{\mathrm{out}}}{P_{\mathrm{in}}} < \left(\frac{2}{\gamma+1}\right)^{\frac{\gamma}{\gamma-1}} \\ 1.379 \cdot \sqrt{\frac{2\gamma}{\gamma-1} \cdot \left(\frac{P_{\mathrm{out}}}{P_{\mathrm{in}}}\right)^{\frac{2}{\gamma}} \cdot \left(1 - \left(\frac{P_{\mathrm{out}}}{P_{\mathrm{in}}}\right)^{\frac{\gamma-1}{\gamma}}\right)} & \text{otherwise} \end{cases} \tag{3.5}$$

$K_{\mathrm{V}}(l)$ is a property of the valve, where $K_{\mathrm{V,max}}$ defines the maximum mass flow for a fully open valve ($l = 1$). The rangeability R is the ratio between a fully opened and closed valve.

However for the LHC Beam Screen, this Samson method has been modified by the cryogenics team to obtain better results in a weakly supercritical regime [19]. The changes are highlighted in the following set of equations.

$$\dot{m} = \mathbf{1.25 \cdot 10^{-5}} \cdot A(\frac{P_{\text{out}}}{P_{\text{in}}}) \cdot \sqrt{\rho \cdot P_{\text{in}}} \cdot K_{\text{V}}(\mathbf{l})[\text{m}^3/\text{h}] \tag{3.6}$$

$$\mathbf{l} = l(u) = 1.1u - 0.1 \tag{3.7}$$

$$\boldsymbol{\gamma} = \frac{5}{3} \tag{3.8}$$

$$A(\frac{P_{\text{out}}}{P_{\text{in}}}) = \begin{cases} 1 \quad \text{if} \quad \frac{P_{\text{out}}}{P_{\text{in}}} < \mathbf{0.42} \\ 1.379 \cdot \sqrt{\mathbf{5.03} \cdot \left(\frac{P_{\text{out}}}{P_{\text{in}}}\right)^{\frac{2}{\gamma}} \cdot \left(1 - \left(\frac{P_{\text{out}}}{P_{\text{in}}}\right)^{\frac{\gamma-1}{\gamma}}\right)} \quad \text{otherwise} \end{cases} \tag{3.9}$$

First of all a different constant is used in Eq. (3.6), $1.25{\cdot}10^{-5}$ instead of 14.2. Secondly, a pre-constraint is applied to the valve in anticipation of the negative thermal expansion during the cooling-down. This is reflected in the expression $l(u)$, where the measured and logged valve opening u is processed to obtain more accurate results. This conversion distorts the meaning of R, as l should normally range between 0 and 1 for minimum and maximum openings, whereas $l(u)$ as in Eq. 3.7 can become negative. In practice however, the electrical heater prevents very low values of u, which remains between 0.15 and 0.98 for a typical fill and translates to values of l that range between 0.06 and 0.98. The approximation of a constant γ is valid for ideal gasses. The critical point of Helium is 5.2 K, while the temperature at the valve is normally around 20 K, which is sufficiently far away. The effects of the changes of the numerical factors in $A(\frac{P_{\text{out}}}{P_{\text{in}}})$ are illustrated in Fig. 3.5.

$$\mathbf{0.42} = \left(\frac{2}{\gamma+1}\right)^{\frac{\gamma}{\gamma-1}} - 0.067 \tag{3.10}$$

$$\mathbf{5.03} = \frac{2\gamma}{\gamma-1} + 0.03 \tag{3.11}$$

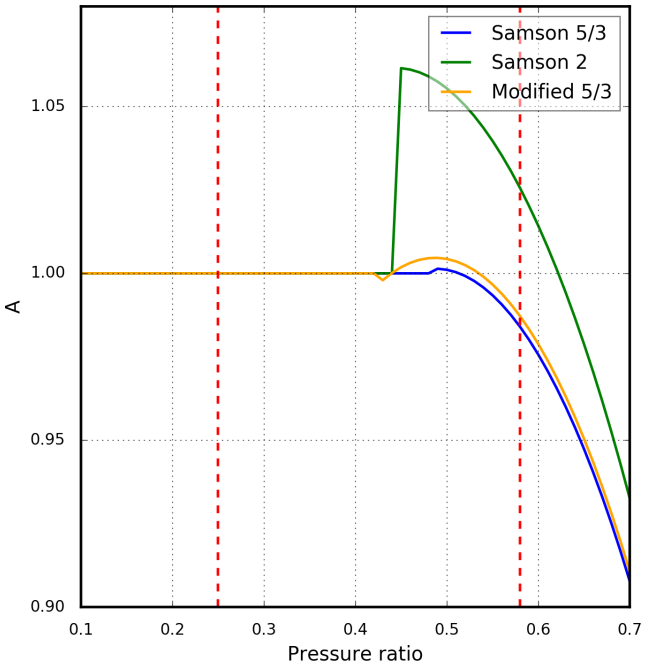

Figure 3.5: These curves illustrate the effect of modifications to the Samson A function. The original function as in Eq. (3.9) is shown for two values of γ, 2 and $5/3$ together with the modified version that is implemented for the LHC cryogenics. In red are shown the limits between which the pressure ratios range for a typical fill.

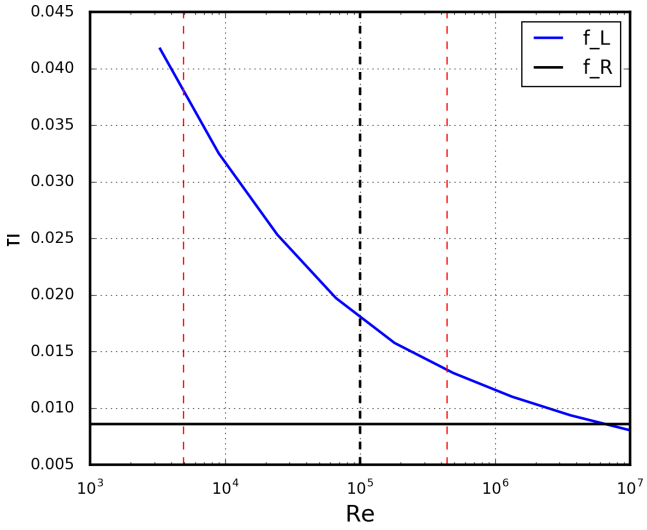

Figure 3.6: The term f_L from Eq. 3.16 is defined in three steps for different ranges of Reynolds number Re. The horizontal line is f_R from Eq. 3.14 for the radius and surface roughness of the Beam Screen cooling pipes is independent from Re. The red lines mark the upper and lower bounds of Re for a typical fill.

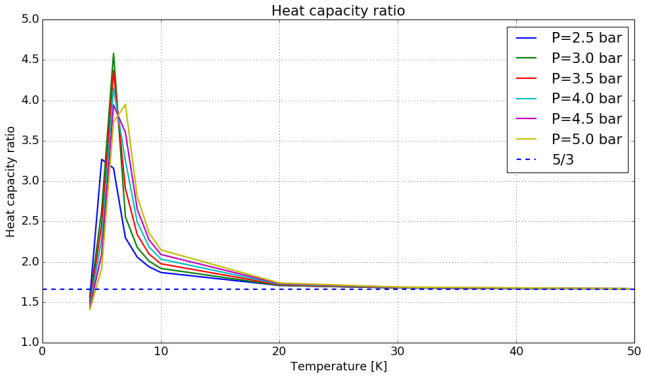

Figure 3.7: The heat capacity ratio γ as in Eq. (3.4) for different pressures and temperatures is obtained by interpolation over tables that have been calculated with HEPAK software [18].

3.2.2 Pressure drop

For the valves in the cryogenic cells of the LHC, the pressure P_{in} in the formulas above corresponds to P_3 in Fig. 3.3 and is not measured. It can be approximated with P_1, as the pressure drop along the Beam Screen is expected to be small (Fig. 3.4). This allows to save a significant amount of computation time and is done for the online calculations for the logging database. For heat loads above ∼100 W, that estimation should however be avoided [17].

The pressure drop through a pipe is calculated with the Darcy-Weisbach equation (3.12), again modified by the CERN cryogenics team.

$$\Delta P = \frac{\max(f_{\text{R}}, f_{\text{L}}(\text{Re})) \cdot L \cdot \dot{m}_{\text{P}}^2}{2r \cdot \rho(P,T) \cdot (\pi r^2)^2} \tag{3.12}$$

$$\dot{m}_{\text{P}} = \frac{\dot{m}}{n_{\text{P}}} \tag{3.13}$$

$$f_{\text{R}} = \left(\frac{1}{2\ln(\frac{r}{R}) + 1.74} \right)^2 \tag{3.14}$$

$$\text{Re} = \frac{2r \cdot \dot{m}}{\pi r^2 \cdot \mu(P,T)} \tag{3.15}$$

$$f_{\text{L}}(\text{Re}) = \begin{cases} \frac{0.3164}{\text{Re}^{0.25}} & \text{for } 3 \cdot 10^3 \leq \text{Re} < 10^5 \\ \frac{0.221}{\text{Re}^{0.237}} + 0.0032 & \text{otherwise} \end{cases} \tag{3.16}$$

The pressure drop depends on the mass flow per pipe $\dot{m}_{\text{P}}$, the helium density ρ, the length of the pipe L, the pipe radius r and the friction factor f. Reynolds number Re, a measure for the flow turbulence which depends on the helium viscosity μ, decides upon the way this friction factor is determined. The two branches in Eq. (3.16) are Blasius correlations. A lower limit is defined by f_R, which is the Colebrook-White equation in the limit of an infinite Reynolds number [20, 21].

Figure 3.6 shows $f_L(\text{Re})$ and f_R for the surface roughness and inner radius of the Beam Screen cooling pipes. Re ranges between $4.9 \cdot 10^3$ and $4.4 \cdot 10^5$ for a typical fill.

Because $\dot{m}$ and ΔP depend on each other, an iterative approach is performed where ΔP starts at 0 ($P_3 = P_1$), and $\dot{m}$ is calculated with Eq. (3.2). P_3 is then found as $P_1 - \Delta P$ and serves as an input for the mass flow again. This is continued until P_3 does not change by more than 1% for an iteration.

3.2.3 Comparison of results

The calculation presented in the previous pages has been implemented in a python module for all the cooling loops installed in the LHC. The obtained results have been validated against the values obtained with the online calculation implemented by the cryogenics team, which are recorded in the LHC logging database. The latter has been computed neglecting the pressure drop, whereas the new module offers a choice but defaults to including this effect.

Figure 6.2 in the appendix shows in a histogram the relative change of the pressure from P_1 to P_3, as it is computed for a typical fill with the new module. These changes do not exceed 15%, and are for the most part well below 5%. As $\dot{m}$ and h_3 from Eq. 3.1 also depend on P_3, different $\dot{Q}_{\text{BS}}$ are obtained.

The cooling powers are compared in Fig. 3.8 for both the arc averages and the family of Q6 quadrupoles. Especially for the high heat load cells in the arcs, the differences due to the inclusion of ΔP are visible but do not exceed 10%. On the contrary, the effect is almost nonexistent for the quadrupoles. This is because the pressure drop depends linearly on the length of the cryogenic cell, and the quadrupole cells are only between 4.8 and 8.6 m long compared to 53 m of the arc half-cells.

It is notable that the logged arc heat loads are different from the recalculated values, even those without pressure drop although they are meant to follow the same algorithm. This is due to a difference concerning how the cells with failing sensors are handled. As noted before, the temperature sensor for T_1 and the pressure sensors for P_1 and P_4 are attached to the supply headers. If one of these sensors fail, it is substituted by the previous one, as these headers cover a whole arc and the temperature and pressure there only changes slowly. These corrections are performed both for the logged and recalculated heat loads. If measured values are missing for another type of sensor, for example T_2 or T_3, the calculations for the corresponding cell is not carried out in the new module. This is currently the case for 16 half-cells in the arcs. While taking the arc averages, these are subsequently ignored. In the code used for the logged data, these sensor values are all set to 0 and the calculation is continued, leading to wrong results for those 16 cells. This in turn distorts the arc averages to the extent visible in Fig. 3.8.

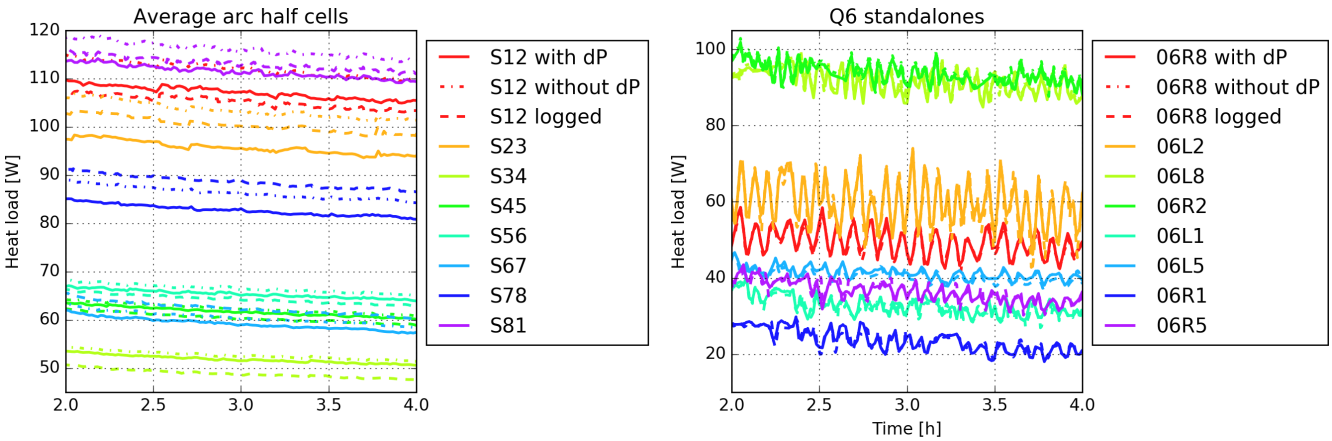

Figure 3.8: The logged and recalculated heat loads for the LHC arcs and Q6 standalone quadrupoles. The lines are not different for the quadrupoles, but show a deviation of up to 10% for the arcs. The quadrupoles do not all have the same lengths. Those in points 2 and 8 (identified by the last character of the label) are 8.6 m long, whereas those in points 1 and 5 are 4.8 m long.

The new module should therefore be used when possible, as it yields more accurate results for the arc averages. Another feature of this module is that it allows for a quick recalculation for all fills of 2015 and 2016 in case the valve configurations $l(u)$ from Eq. (3.7) or $K_{V,\max}$, R from Eq. (3.3) are updated, or in case any other changes to the calculations are deemed necessary. For the LHC logging system it is not foreseen to change data once published.

All properties used for the heat load recalculation of the typical fill 5219 (see also Fig. 1.3 are given in the appendix (Sec. 6.2) as histograms. These are formed out of the values from all time steps and all cryogenic cells in the arc. Additionally, only the values at one point in time at high energy are shown, as these are the most relevant ones.

3.3 Specially instrumented cells

Three specially instrumented cells in arc 45 are equipped with additional temperature sensors between the four main magnets, see Fig. 3.9. Their names are 13L5, 33L5 and 13R4 according to the nomenclature that is used for the heat loads on the CERN logging data base[3]. In the last Extended Year-End Technical Stop (EYETS), a dipole had to be exchanged in arc 12 and the whole sector has been warmed up. This made it possible to install additional instrumentation in one of its cells. Once the operation in 2017 has started, this cell will be added to the analysis.

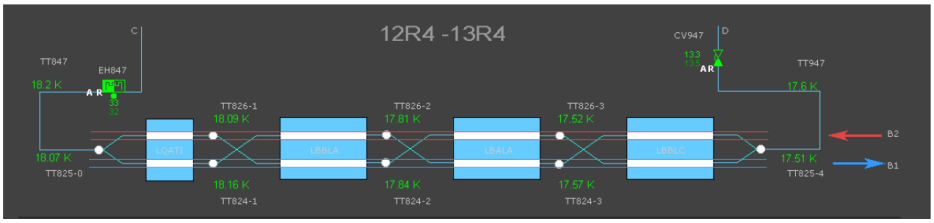

Figure 3.9: Additional temperature sensors between the main magnets are installed in the specially instrumented cells [22].

The heat load calculation for a single magnet is similar to Eq. (3.1), except that the heater and the static sink-in heat loads are not necessary. The mass flow is determined for the whole cell with Eq. (3.6) while neglecting the pressure drop. This could be added to achieve slightly better results. The enthalpy difference is again obtained by interpolating helium property tables.

$$\dot{Q}'_{\mathrm{BS}} = \dot{m} \cdot \Delta h \tag{3.17}$$

The pressure drop at each magnet is not taken into account for these cells, as the pressure is unknown at four spots. It would certainly be possible to find an approximation, for example a linear drop from the pressure P_1 to P_3 (following

[3] The pressure and temperature sensors follow a different naming convention, where these cells are called 12R4, 32R4 and 13L5, respectively.

the notation of Fig. 3.3) along the helium line, but this is not currently implemented. P_1 is used at all points instead. Unfortunately a temperature sensor is broken for the cell 33L5, which means that it is not available for analysis.

Figure 3.10 demonstrates the heat loads for a typical fill. Several issues and observations can be immediately identified:

- The recalculated heat loads for the full cell and the sum of the components do not match, the reasons for which are still unclear. Furthermore, the logged values for the cell heat load are very different from the recalculated ones for both cells. These issues need to be followed up together with the cryogenics team.
- The quadrupole for cell 13R4 has negative heat load, this means the helium after this device is measured to be colder than before. This could indicate that there is a heat transfer to the 1.9 K cold mass or that a sensor is wrongly installed or faulty.
- The dipoles, even though identical, yield much different heat loads. This is consistent with the fact that the cells in the LHC show a huge variety in their heat loads. It would be surprising if the dipoles would not show a spread.
- The quadrupole heat loads (after an offset correction) are very low, in the order of a few W/m. The measured heat loads from the Q6 standalone magnets with similar beam screen size are much higher (see Fig. 3.8), a contradiction which is not yet resolved. It could either mean that the measurements are completely wrong for either the family of standalones or for the two special quadrupoles. Alternatively the heat loads could be really different by a large factor that can currently not be explained. This would have a large impact on our understanding of electron cloud. Figure 3.11 demonstrates how the different components would be shared if the dipoles in the arc cells were behaving like the average of the Q6 family.
- The dipole heat load increases significantly during the beam energy ramp, while it barely changes in case of the quadrupoles.

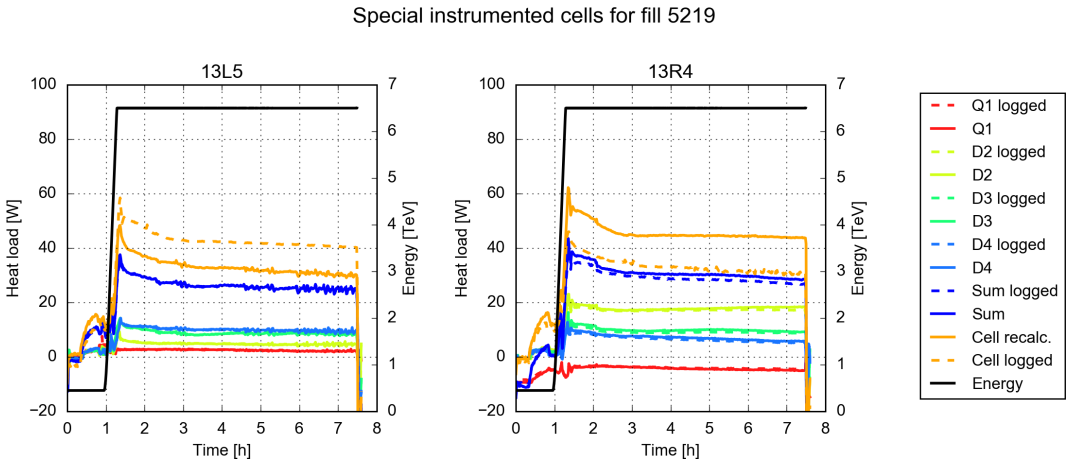

Figure 3.10: For the special instrumented cells, the heat loads of the 4 magnets and the sum are shown. Furthermore the energy of the beam is displayed at the secondary axis. The proton injection takes place in the hour before the energy increase. The recalculated as well as the values form the logging data base are shown. They agree very well for the magnets themselves, whereas they contradict for the full cell when the special sensors are part of the calculation.

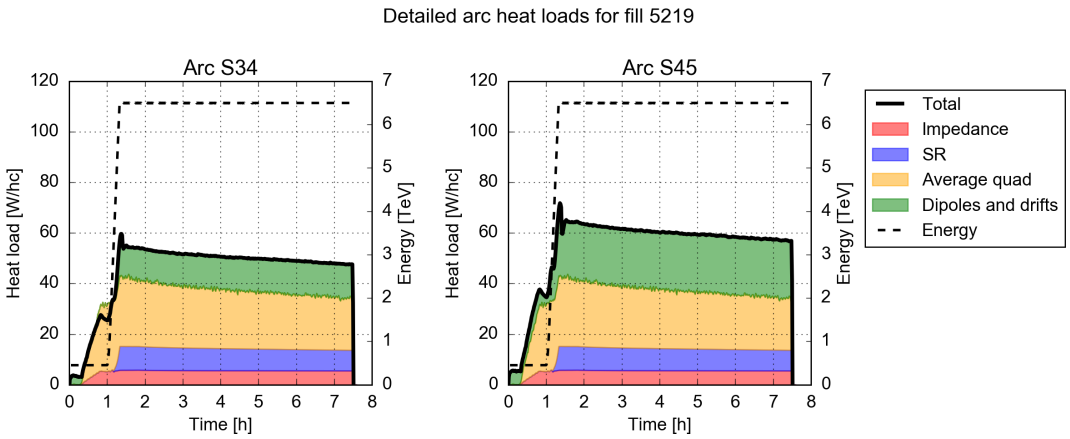

Figure 3.11: Under the speculative assumption that the quadrupoles in the arc cells have the same heat load per m as the standalone Q6 quadrupoles, the different heat load components can be assigned as in these plots. As a consequence, the differences between the arc of the LHC are solely due to the dipoles and interconnections. The same plot for the other arcs is given in Fig. 6.5 in the appendix.

3.4 Estimations of heat loads from other sources

The measured cooling powers that have been subject to this chapter so far include all sources of heat load from the beam, also those that are not related to electron cloud. Therefore, the expected contribution of the resistive wall effect (impedance) and synchrotron radiation is calculated and subtracted. It was implemented as a small python module[4], the coding was done by the author of this report and Giovanni Iadarola.

For the resistive wall effect, classical single bunch formulas as typically done by the CERN impedance team are used [23].

$$P = \frac{1}{C}\Gamma\left(\frac{3}{4}\right)\frac{M}{b}\left(\frac{N_b e}{2\pi}\right)^2\sqrt{\frac{c\rho(T)Z_0}{2}}\sigma_t^{-3/2} \tag{3.18}$$

The following quantities are involved:

- The LHC circumference C.
- The number of bunches M, the particles per bunch N_b and the average bunch length σ_t, which are obtained by Fast Beam Current Transformer (FBCT) measurements and logged. Note that the logged bunch length corresponds to a 2 σ diameter.
- The beam screen half height $b = 18.4$ mm.
- The fundamental constants e, c and Z_0.
- The surface resistivity of the beam screen ρ, where a beam screen temperature of 20 K is assumed.

The surface resistivity of the beam screen is the temperature dependent surface resistivity of copper $\rho_{\mathrm{Cu}}(T)$ (see Fig. 3.12) with corrections from the magneto-resistive wall effect ($\Delta\rho(B)$) and the stainless steel beam screen weld (f_{w}).

$$\rho(B) = f_{\mathrm{w}}\left(\rho_{\mathrm{Cu}}(20\ \mathrm{K}) + \Delta\rho(B)\right) \tag{3.19}$$

$$\Delta\rho(B) = 10^{-2.69}\left(B\,\frac{\rho_{\mathrm{Cu}}(273\ \mathrm{K})}{\rho_{\mathrm{Cu}}(4\ \mathrm{K})}\right)^{1.055} \tag{3.20}$$

$$f_{\mathrm{w}} = \sqrt{\frac{\rho_{\mathrm{SS}}(20\ \mathrm{K})}{\rho_{\mathrm{Cu}}(20\ \mathrm{K})}}\cdot\frac{l_{\mathrm{w}}}{2\pi b} \tag{3.21}$$

In the last equation, ρ_{SS} is the surface resistivity of stainless steel, which is taken as $6{\cdot}10^{-7}$ Ωm at 20 K, and l_{w} is the length of the weld, which takes up a fraction of 1/60 of the total beam screen circumference.

[4] Available under `https://github.com/giadarol/HeatLoadCalculators`

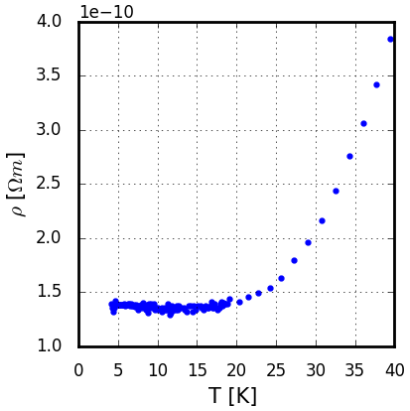

Figure 3.12: The data from which the surface resistivity of copper $\rho_{\mathrm{Cu}}(T)$ is obtained through interpolation. It does not change by much over the temperatures that occur at the beam screen. These range between 4 and 20 K [24].

The synchrotron radiation effect is easier to estimate. Since it is a closed system, the full power of the emitted radiation has to be absorbed by the cooling circuit. The formula for the energy loss per turn is found in standard text books such as [25].

$$\Delta E = \frac{e^2}{3\epsilon_0}\frac{1}{(mc^2)^4}\frac{E^4}{R} \tag{3.22}$$

Here, E is the energy and N the total number of particles of the beam, while m is the proton mass and ϵ_0 the vacuum permittivity. The radius R is the bending radius of the dipoles, not to be confused with the average machine radius. To obtain the power, this has to be scaled with the revolution frequency f_{Rev} and the number of particles in the beam N.

$$P = N \cdot f_{\mathrm{Rev}} \cdot \Delta E \tag{3.23}$$

The synchrotron radiation is only taken into account for the arcs since strong bending magnets are not installed elsewhere. It is assumed to be distributed uniformly across the cryogenic cells.

For a typical fill, the contributions of the modelled heat loads are shown in Fig. 1.3. The synchrotron radiation heat load has a larger effect than the impedance heat load.

3.5 Validation and error analysis

The error analysis of the heat load measurements is being investigated by cryogenics team. The current status was presented in December 2016 [22]. These efforts are quite relevant for this report, so they are in part briefly described here. Some additional data analysis is reported to validate the results of the modelled contributions of synchrotron radiation and the resistive wall effect.

Figure 3.13 demonstrates the error propagation of two parameters in the calculation from Sec. 3.2 on the resulting heat loads. These are the rangeability R and the maximum gas flow trough the valve, $K_{\mathrm{V,max}}$. The possible relative errors of up to 60% are quite alarming at first, but this is merely an arithmetic example of what would happen if these parameters were wrong by up to 30% each.

On the other hand there have also been dedicated measurements to validate the heat loads. These are briefly described in Fig. 3.14 and have been performed for the arcs 12, 23 and 78 in 2016. The bottom line is that even though individual cells can deviate by up to 30% for a typical fill, there is no systematic error towards lower or higher heat loads and the average arc heat loads are deemed accurate by 3%. However this only holds for the typical valve openings as they are encountered in operations.

The combination of synchrotron radiation and impedance heat loads can be compared with the measured cooling power for fills where no significant electron clouds are expected. The best candidate for these are fills with 100 ns bunch spacing, these have last been performed in 2015. Figure 3.15 shows the cell by cell heat load at collision energy as well as the corresponding model heat loads. The average arc heat loads are in very good agreement with the expectations to the extent of less than 1 W. This is true for all arcs. Other plots are shown in the appendix of this report: Fig. 6.6 and 6.7. This being said, large varieties and outliers between cells are present. It is unclear whether these are due to measurement artifacts, for example because there is a thermal coupling with reservoirs at lower or higher temperatures.

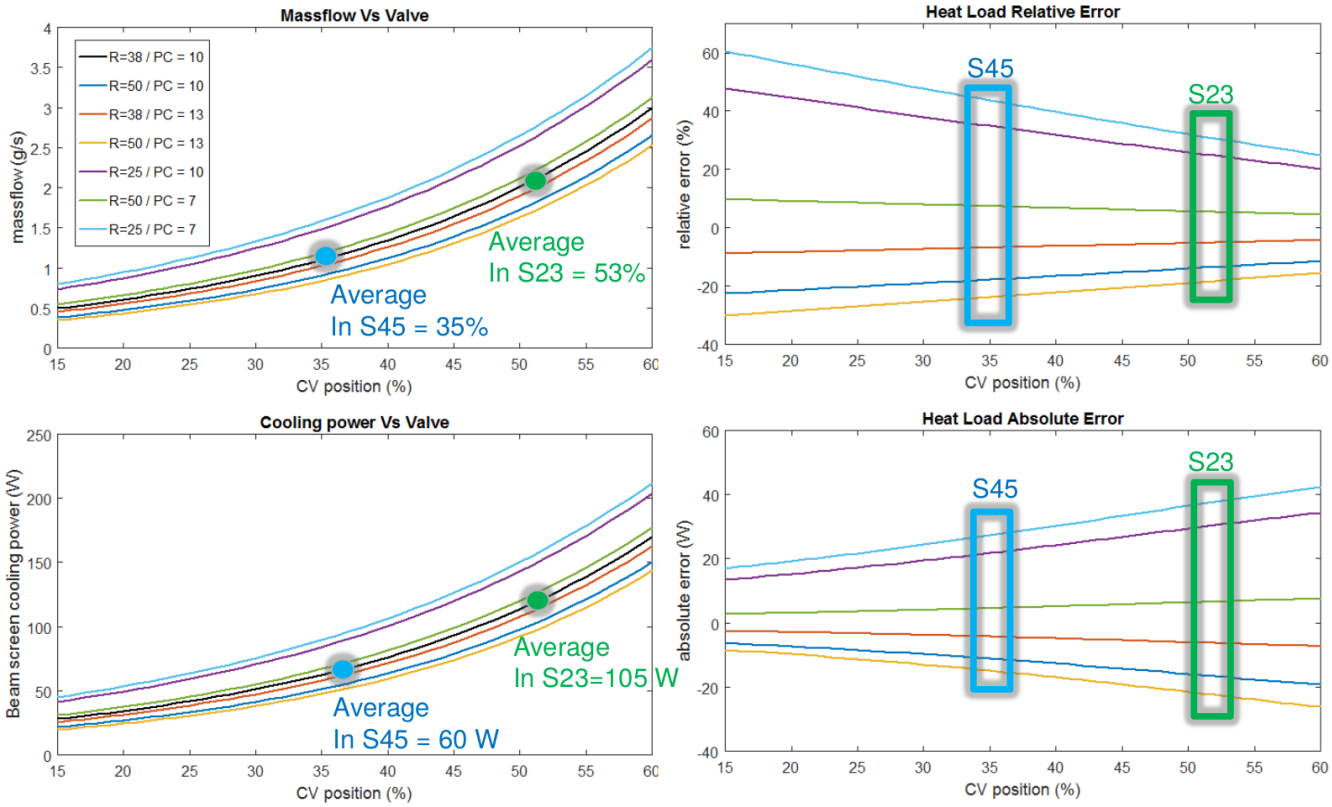

Figure 3.13: The effect of wrong parameters on the calculation presented in Sec. 3.2 is analyzed here. The valve rangeability R from Eq. 3.3 and the pre-constraint PC (the latter being the subtracted term from Eq. 3.7) are being varied by 30% to find out the effect on the resulting heat load. R is defined in the configuration files and assumed as 38 for most cells, while PC is hardcoded as 0.1. The CV position on the x axis corresponds to u from Eq. 3.7. The two plots on the left demonstrate by how much the mass flow and heat loads change for various combinations of R and PC. The blue and green dots indicate the average valve positions of sectors 45 and 23, a low and a high heat load sector (as in Fig. 1.3). On the right, the possible stretch of the results is shown. The impact is larger on low heat loads cells in relative terms, while the opposite is true in absolute terms.
This is a slide taken from a presentation, where a member of the cryogenics team described the ongoing efforts to validate and improve the heat load measurements [22].

Another point to make is the importance of subtracting the offset for low heat load fills. Fig. 3.16 shows how these are found for the 100 ns fill that was featured above. In case this step is omitted, the resulting histograms for 2 arcs can be compared in Figs. 6.7 and 6.8. Not only is the spread between the cells much larger than before, but also do the modelled and measured cooling powers differ by a large amount.

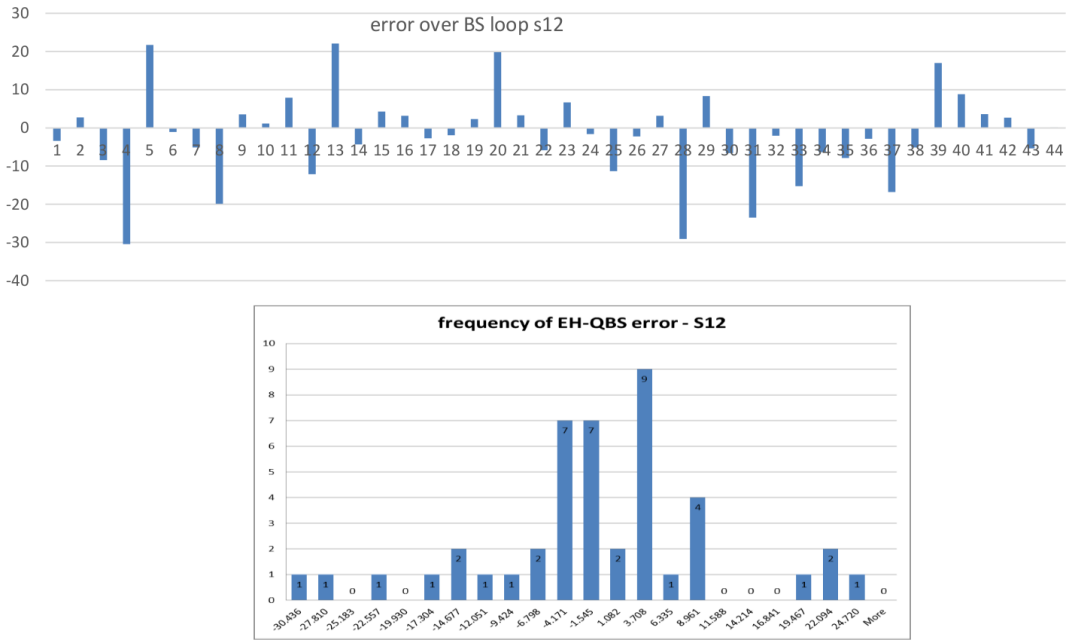

Figure 3.14: The measured beam screen temperatures and valve openings from a typical fill have been reproduced with the electrical heater that is installed in every cell (see Fig. 3.3). The power of the heater is then compared with the measured heat loads, and the deviation is shown in the top plot in relative terms for all cells in the arc 12, which requires among the highest cooling power in the LHC. The bottom plot shows a histogram of these deviations. For the most part, these are rather evenly distributed towards both sides. There are 3 cells with a deviation between -20 and -30% but also 4 cells between +20 and +25%, for example. These plots origin from [22], as well.

Figure 3.15: The cell by cell heat loads for a fill with 100 ns bunch spacing are shown here. As the electron cloud is not expected to be relevant for this fill, the heat loads should match the combination of synchrotron radiation and impedance.

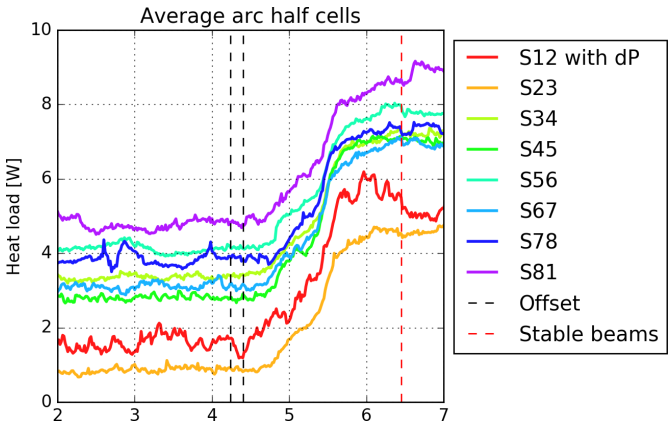

Figure 3.16: This plot corresponds to the same fill as Fig. 3.15 and is meant to explain how the heat load offsets are found. The second vertical black line marks the begin of proton injection. The average of the quarter hour between the two black lines defines the offset that is subtracted from the cooling power for the whole fill. The red line indicates the moment where "stable beams" are declared.

4 Heat load observations

The data from the LHC instrumentation, including the parts relevant for electron cloud studies, are available in the CERN logging database. Although this data can be accessed easily, the comparison of beam or heat load properties between more than just a few fills used to be tedious. One reason is that the data for a fill is stored together in a file which had to be read as a whole even when only a small part of it was needed. To allow for a better data analysis, a tool was developed that greatly increases our data analysis[1]. This tool itself is presented in this section. Later on, an important process called beam induced mitigation of the electron cloud is first explained and then evaluated for the LHC during 2015 and 2016. Furthermore, the results of a Machine Development session dedicated to investigating the effect of different bunch intensities on heat loads are presented. These allow an estimation of the scaling of electron-cloud effects for intensities up to $1.1 \cdot 10^{11}$ particles per bunch.

4.1 Data dictionary

The main output of the implemented module is a nested python dictionary with self-descriptive keys. It contains data for 282 fills, those that have reached the stable beams status in 2015 and 2016. For each of them, the following properties are stored:

	Once or	multiple times per fill	Note
Fill number	x		e.g. 5219
Filling pattern	x		e.g. '25ns_2220b_2208_1940_2036_96bpi_24inj'
Top energy	x		
Bunches per injection	x		Bunches per injection from the SPS
Heat load offset	x		For all cells and the arc averages
Sum of fill heat load	x		For all cells and the arc averages
Heat loads		x	For all cells and the arc averages
Heat load from Imp./SR		x	For both beams
Time points		x	In seconds after 1970 (Unix time)
Average bunch length		x	For both beams, from FBCT
Bunch length standard deviation		x	For both beams
Number of bunches		x	For both beams, from FBCT
Total intensity		x	For both beams, from BCT

Some of the parameters need further clarification.

- The recalculated heat loads and model heat loads from Sec. 3.2 and 3.4 are used.
- The heat load offset is the average of the recalculated heat load between the proton injection ("Injection Physics Beam") and 15 minutes before, this means before there is beam in the machine, see also Sec. 3.5.
- The integral of the fill heat load allows us to estimate the amount of electron bombardment must have taken place. Later on this quantity is compared with the decrease in heat load.
- The bunch length is stored as the diameter of a 2 σ beam, it therefore corresponds to the 4 σ beam length.
- The filling pattern is an identifier for the arrangement of filled and empty bunch slots for a given fill.
- FBCT is the acronym for Fast Beam Current Transformer.

The time points for the parameters that are stored several times per fill is listed here, they correspond to what is also shown in Fig. 1.3.

- The beginning of the fill.
- The beginning of the proton injection, which corresponds to the "Injection Physics Beam" mode.
- The beginning of the energy ramp.
- The end of the beam size squeeze process.

[1] This python module is available online under `https://github.com/pdijksta/hl_dicts`

- The declaration of stable beams.
- Every hour afterwards for up to 24 hours.

The basic properties of the fills that are stored in the heat load dictionary are shown in Fig. 4.1.

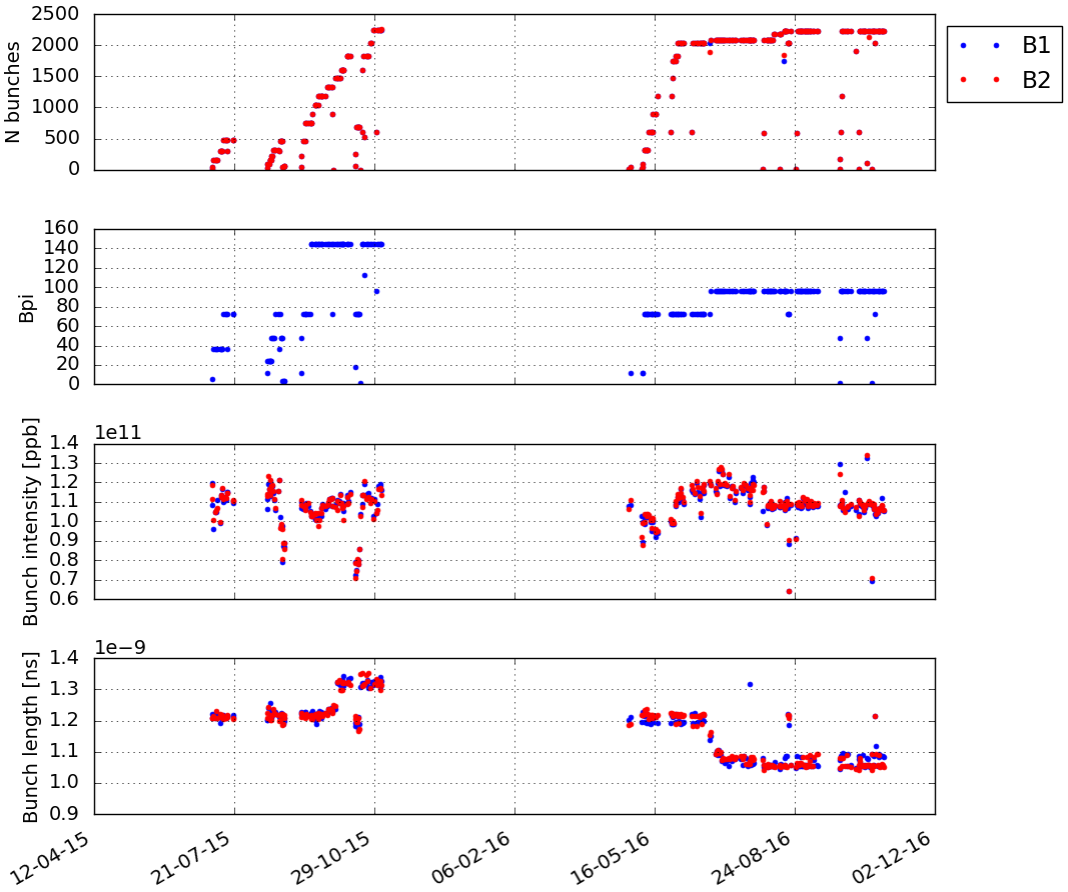

Figure 4.1: Basic beam properties are shown for all fills that are contained in the dictionary. The number of bunches for the two beams is identical for almost all fills, the red and blue dots overlap. Bpi is short for bunches per injection, a measure which corresponds to the length of the trains.

4.2 Electron cloud mitigated scrubbing in 2015 and 2016

The secondary electron emission of surfaces that are exposed to electron irradiation tends to decrease gradually. This effect is called "scrubbing" or "SEY conditioning". In the case of electron clouds, it means that they can be self-mitigating. Dedicated measurements have taken place for example at the SPS, these show a rapid decrease of electron emission after only a few hours. This process however slows down considerably as it can be seen in Fig. 4.3, where much longer time intervals are necessary to decrease the SEY curve by roughly the same amount.

In the case of the LHC, there are no measurement devices installed to observe electron clouds directly. The analysis from this section is focused on the how the arc heat loads have changed during the scrubbing that occurred during the proton physics fills in 2015 and 2016. Fills with less than 800 bunches per beam were excluded. For all following plots, the heat load is shown at the end of the squeeze process. The model heat load from impedance and synchrotron radiation has not been subtracted. Figure 4.3 first displays the heat loads as they have been measured. Because of much less bunches for the earliest fills of 2015, this plot alone would be misleading as the heat loads are rising by a great amount. A second plot, where the heat load is normalized to the total beam intensity, reveals that the electron cloud effects are strongly decreasing for the whole year of 2015. This trend continues in 2016, albeit at a much slower rate.

While looking at the third plot, it turns out that the differences between the arcs has only barely decreased in 2016. Apparently there is a cause of heat load generated by a source that scales with the beam intensity and is not affected by electron-cloud mitigated scrubbing.

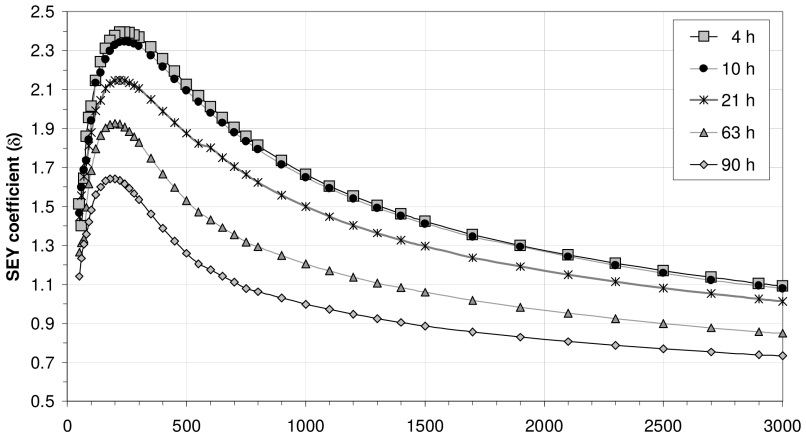

Figure 4.2: A copper sample has been exposed to a beam similar to the ones at LHC. The measured secondary emission yield changes with the duration of exposure. This data has been taken in the SPS [26].

Figure 4.4 shows a very similar plot, where the half-cells in the arcs are not grouped by the arc they are located in, but according to the cooling power they required for the last ten fills of 2016. Every of these "deciles" corresponds to the average of about 37 cells, which are relatively similar to each other. It becomes clear that the difference between these cells in normalized heat load traces back to at least the beginning of operations in 2015.

The next figure (Fig. 4.5) then relates the measured heat loads to the sum of the heat loads from all previous fills. Here, also the dipoles from the specially instrumented cells and the Q6 quadrupoles are shown. For the arcs and for the deciles, it is clear that the cells that correspond to the high heat load curves do not condition faster even though their measured heat load is far higher. It appears to be some kind of offset that they cannot overcome. The reasons for this are yet unclear and will be subject to further studies.

The data for the quadrupoles is very different, but has not been thoroughly studied yet. Only two of the quadrupoles show a notable change in heat loads. It might be that the others have already arrived at their final plateau before 2015. This needs a more careful analysis, however. The data for the dipoles from the special cells on the other hand is compatible with the findings from the arc averages and deciles.

The question came up whether this difference between the cells mentioned before could be caused by an impedance effect. From the side of the impedance team this is regarded as unlikely, but is being further investigated [27, 28]. The next section of this report shows that the electron cloud generated heat loads do scale linearly with intensity in the current regime.

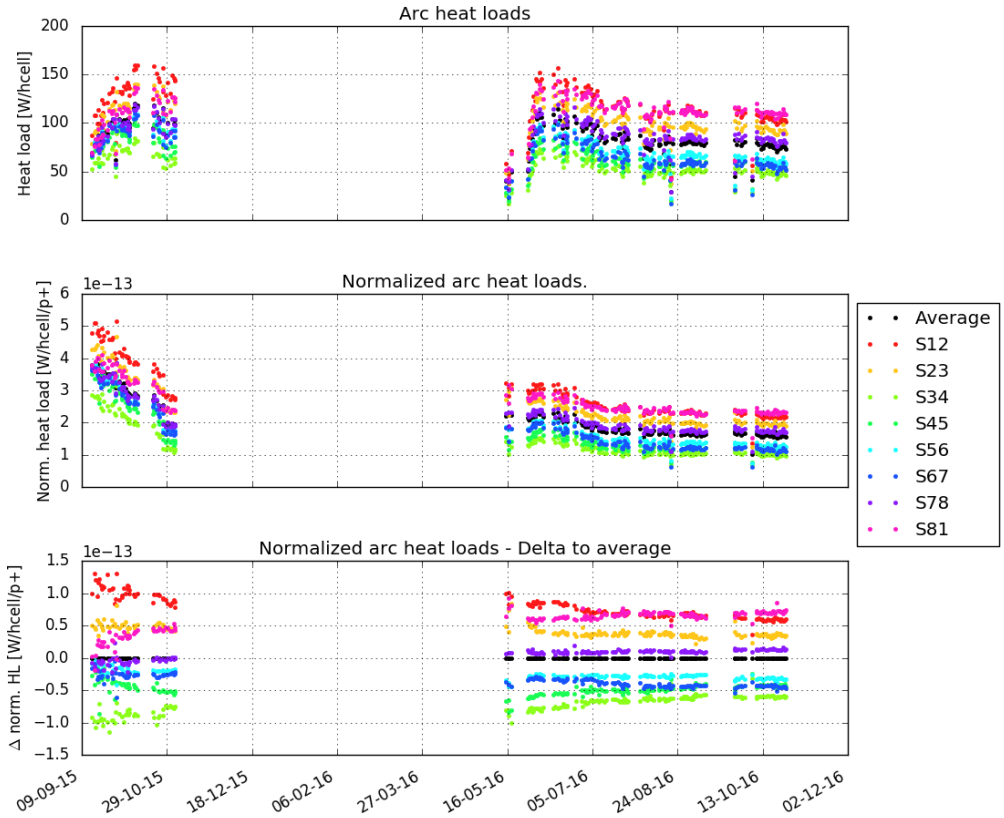

Figure 4.3: The measured average arc cooling powers are plotted in absolute terms in the top plot, while they are normalized with the beam intensity in the middle plot. The bottom shows the differences in normalized heat load with respect to the average value.

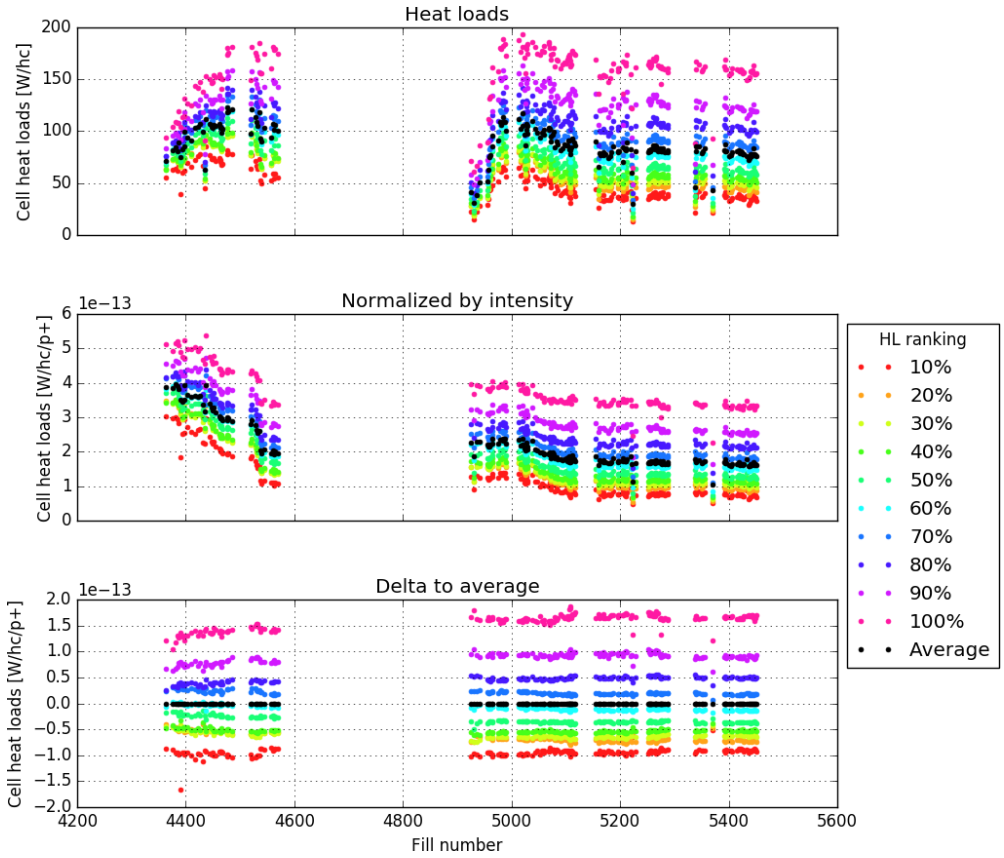

Figure 4.4: Instead of being grouped into arcs, all the cryogenic cells are ranked with respect to the cooling power they required in the last ten fills of 2016. This plot demonstrates that this hierarchy has been present from early on. Relative to each other, the differences in normalized heat load barely changes.

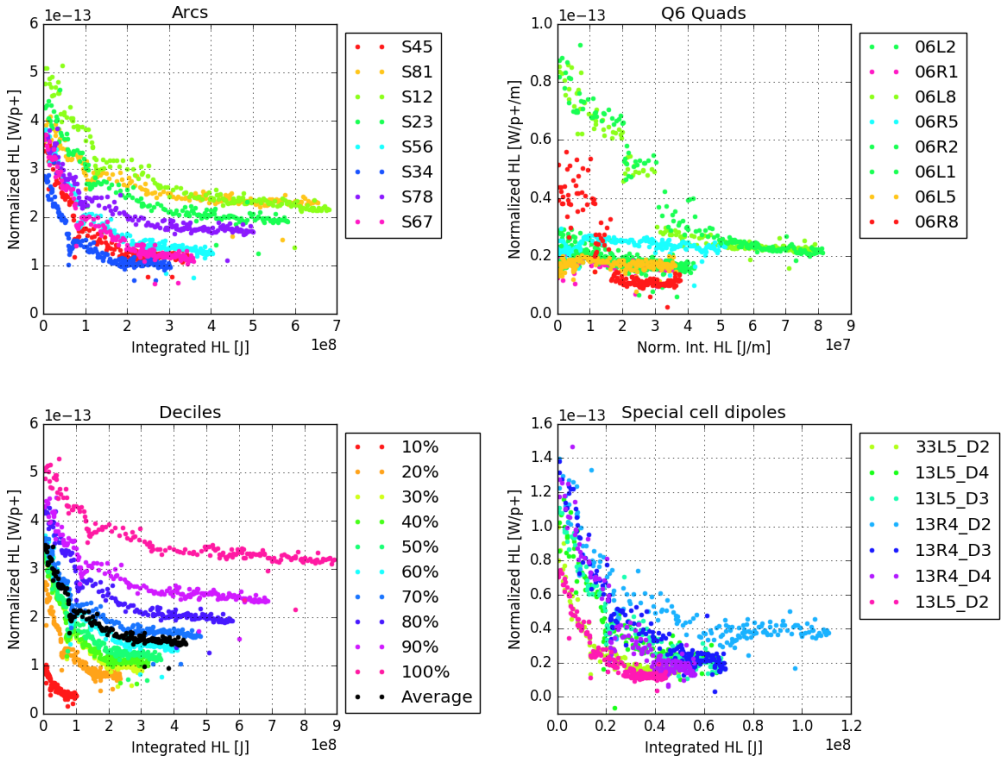

Figure 4.5: The normalized heat loads are plotted against the sum of the heat loads of previous fills since 2015. The special cell dipoles and the Q6 standalone quadrupoles are shown on the right. The plot for the latter is normalized also by the length of the respective quadrupole.

In August 2016, three fills have been performed during an Machine Development session, with the purpose of investigating the dependence of e-cloud build-up on the bunch intensity of the circulating beam. These three fills (5219, 5222 and 5223) were identical in terms of filling schemes and RF settings, but possessed different injected bunch intensities (respectively $1.11 \cdot 10^{11}$, $0.9 \cdot 10^{11}$ and $0.7 \cdot 10^{11}$ p/bunch).

Figure. 4.6 (left) shows the bunch length at high energy against the bunch intensity. The initial value of the bunch length was about 1.2 ns for all fills. The right plot shows the evolution of the heat load at high energy plotted against the bunch intensity. It is notable that for each sector the measurements from the three fills seem not to lie on the same line. This is due to the fact that the bunch length at the end of each fill is significantly shorter than at the beginning of the following one, which increases the electron cloud effects.

In Fig. 4.7, the heat load measured for the same bunch length of 1.15 ns is compared, as indicated by the black lines in Fig 4.6. The uncertainties for this plot consist of 5% of what has been measured, in addition to the offset (see Sec. 3.5), but should be considered as preliminary. In contact with the cryogenics team, a final stance on how the uncertainties should be specified will be found and used for the work leading up to the Master's Thesis.

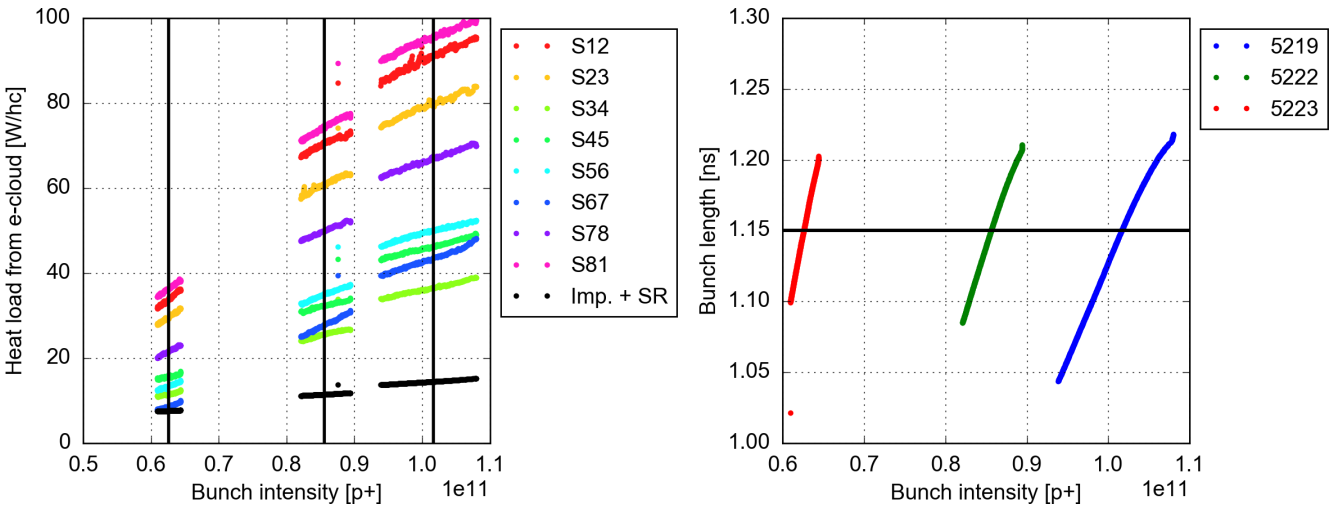

Figure 4.6: The Heat loads as a function of the bunch intensity for the three test fills with different initial bunch intensity are shown on the left. The estimated heat loads from the beam screen impedance and from synchrotron radiation are subtracted and indicated in black.

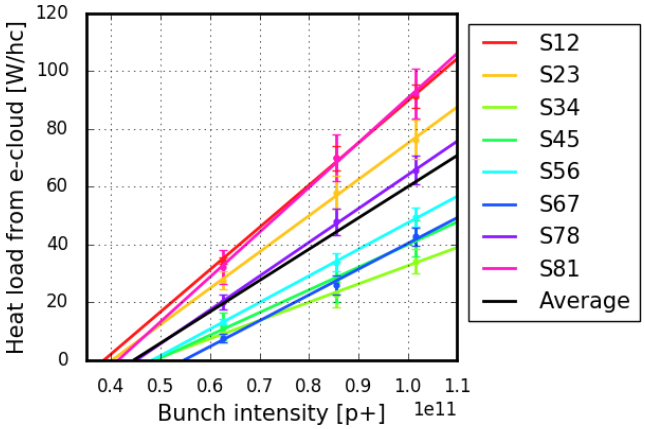

Figure 4.7: The heat loads from the figure above are shown together with a linear fit.

5 Proposed future work

The report gave a description of the work that has been performed in order to improve the understanding of electron cloud effects at the LHC. This final part briefly recaps these steps and points out what should be done in the months to come. While major parts concerning data analysis have been finished, emphasis will be put especially on performing buildup simulations.

5.1 Buildup simulations

The buildup simulations for electron clouds rely on the secondary emission model, which defines how electrons interact with the chamber. The dependence of this model on various input parameters has been studied, see Sec. 2.3. As a next step, simulations based on measured beam parameters have to be performed.

A suitable fill is presented in Fig. 5.1, which shows the total intensity, the average arc heat loads and the bunch length. This data changed significantly over the duration of the fill, and should in principle be reproduced with simulations. The vertical bars indicate interesting points in time along the fill. Simulations using the measured bunch lengths and intensities at these points have already been performed, but not been analyzed to date.

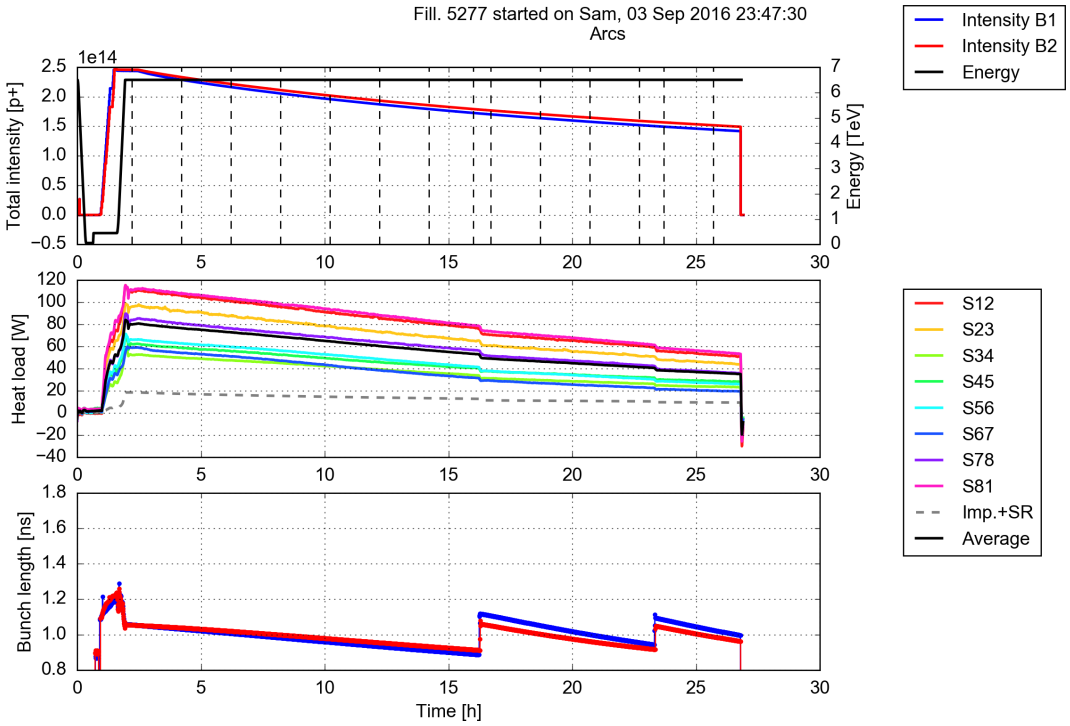

Figure 5.1: Simulations based on this fill will be analyzed to show in which way the modelled electron cloud effects depend on beam parameters such as intensity and bunch length. On two occasions, the bunch length has been increased which is reflected in a sudden change of heat load.

Another necessary step is the formation of a more accurate model of the cryogenic cells in the LHC arcs. The simulations presented earlier in this report covered dipoles and quadrupoles. This has to be extended to the magnet interconnections, which take up about 7 out of 53 m of a cryogenic cell. This space is filled with drift space and correction magnets, some of them of higher order such as sextupoles and octupoles. As such multipoles have not been simulated yet within PyECLOUD, the code will be extended in this aspect.

Furthermore, photoemission by synchrotron radiation will be used as a seeding mechanism for buildup simulations, in place of an initial distribution of primary electrons in the chamber. Measurements taken at CERN with the materials used in the LHC are available, these describe the photon reflectivity and electron yield per impinging electron [29].

Because the cooling power required for the beam screens of the cryogenic cells is the most important indication for electron cloud effects at the LHC, a large part of this report has been dedicated on data analysis and improvement. A module for recalculating the heat loads for all fills in 2015 and 2016 has been written, see chapter 3.2. It includes the effect of the pressure drop, especially relevant for cells with high heat loads. Furthermore, the average arc heat loads are now correctly calculated, ignoring the cells that do not have a full set of functioning sensors. Additionally, specially instrumented cells that allow for a heat load calculation of individual magnets in the arcs have been analyzed (Sec. 3.3). Heat loads from sources other than electron cloud are synchrotron radiation and impedance. These contributions have been calculated and a good agreement is found with the measured cooling powers for fills with very low electron cloud effects (Sec. 3.4 and 3.5). The module for the cooling power recalculation has to be finalized in coordination with the cryogenics team. This will put an uncertainty estimation for these heat loads in place, so they can be compared to simulation results.

The heat load dictionary presented in Sec. 4 has been very helpful in estimating the electron cloud mitigated scrubbing for the previous two years. It was shown that there are several types of cryogenic cells, according to the amount of heat loads measured. It cannot be expected that the differences between these cells decrease as the scrubbing continues in 2017 and beyond. This could have implications for the HL-LHC upgrade. Furthermore, heat loads from three fills with different bunch intensities have been analyzed, in order to find out about the dependence in the current regime of operations at the LHC (see Sec. 4.3).

The LHC will continue its operation in the following months. In the beginning, the heat loads are expected to be higher than towards the end of 2016. This is because the surface properties usually reset to a certain extend and lead to higher secondary emission yields when they are exposed to the beam again after a pause of several months. Therefore, dedicated "Scrubbing runs" [30] will be performed. These are fills which are designed to create strong electron cloud effects, so that the surfaces quickly recondition and allow operation with the nominal beam parameters. The data that is going to be accumulated will be analyzed, especially for the arc that has been warmed up to exchange a dipole in the last shutdown. Because the beam screens in this arc have been exposed to air, it will be very interesting to see the change in heat loads.

6 Appendix

6.1 Heat load calculation template

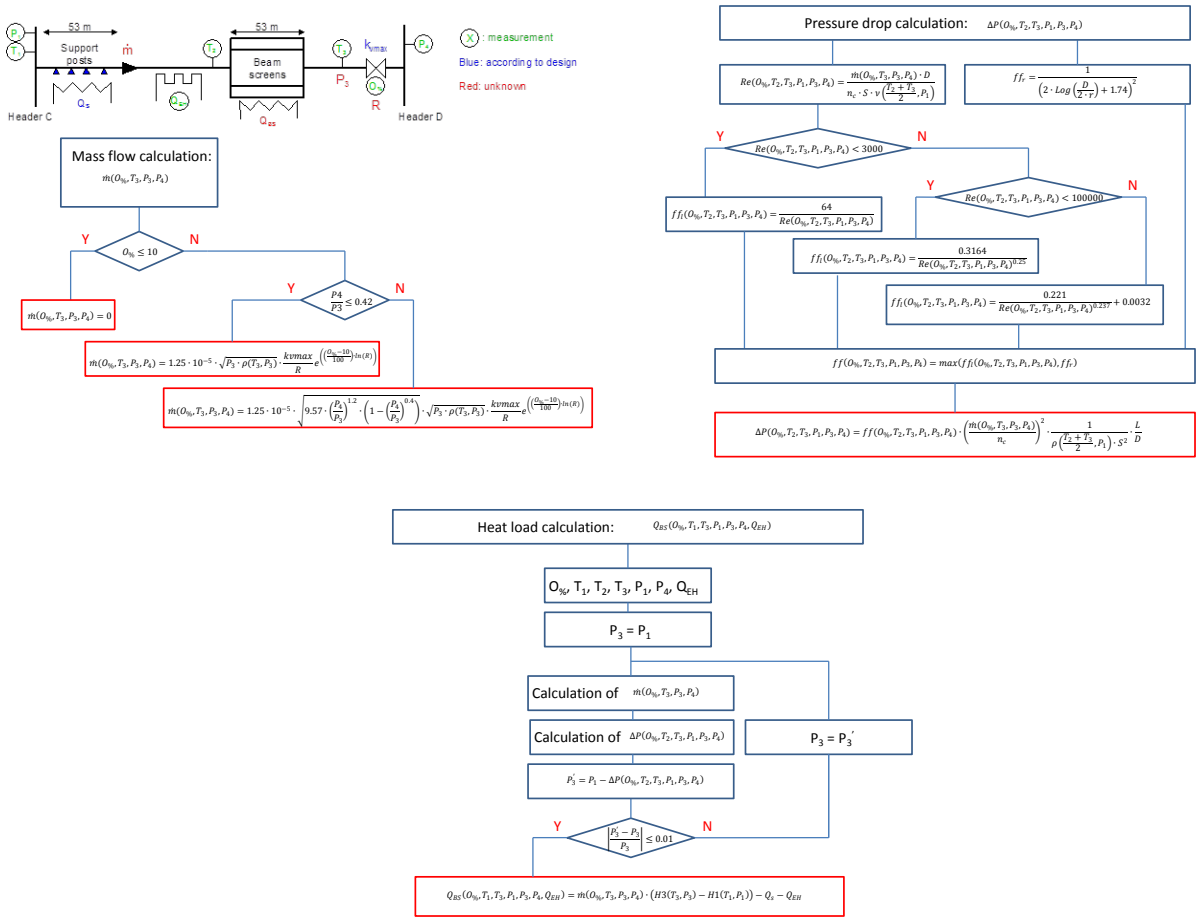

Figure 6.1: The CERN cryogenics team based the heat load computation on these slides by Laurent Tavian [31].

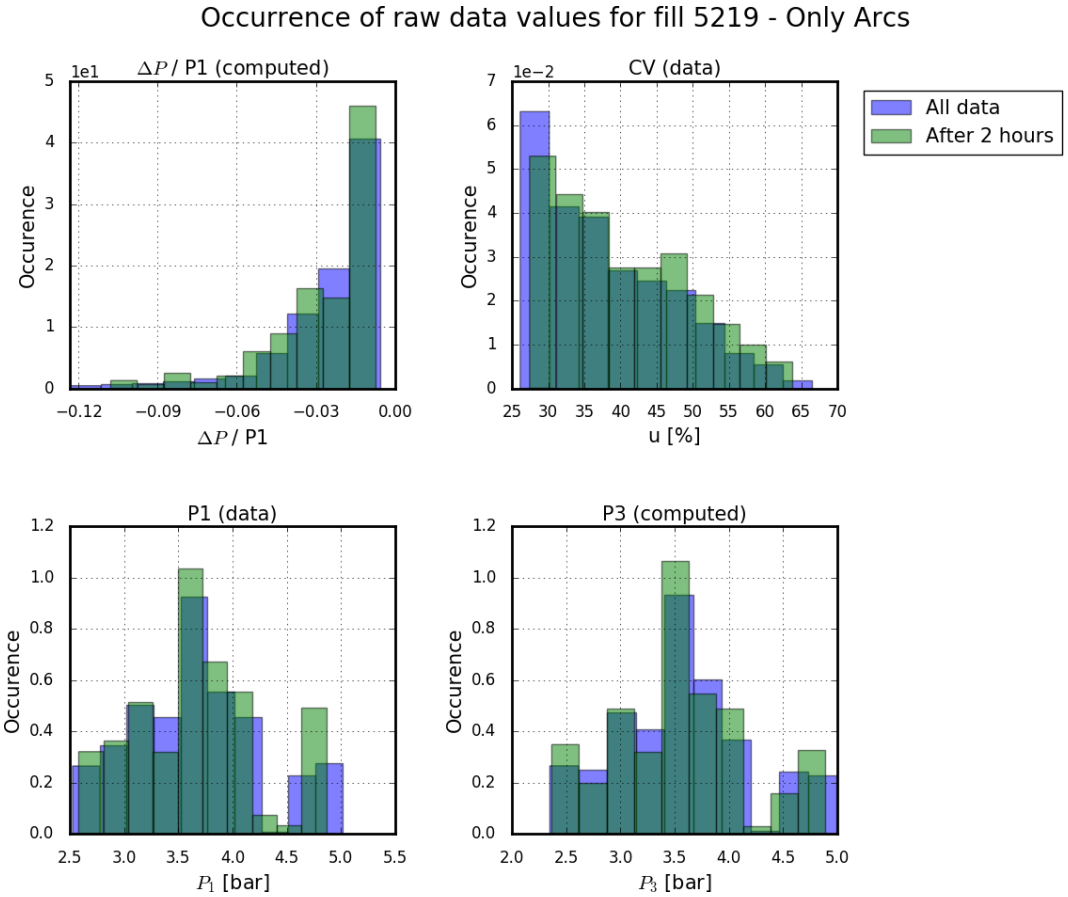

Figure 6.2: How often do certain values relevant for the heat load calculations appear for a typical fill? The data for the blue histograms consists of all points (every 60 s) from the heat load calculation of the arc cells of a typical fill. The green histogram shows only the values for one time point 2 h after the begin of the fill, and is therefore a subset of the blue one. If (data) is appended to the title of a plot, it means that is is a value directly from the logging data base. Otherwise it has been an intermediate or final step of the heat load calculation.

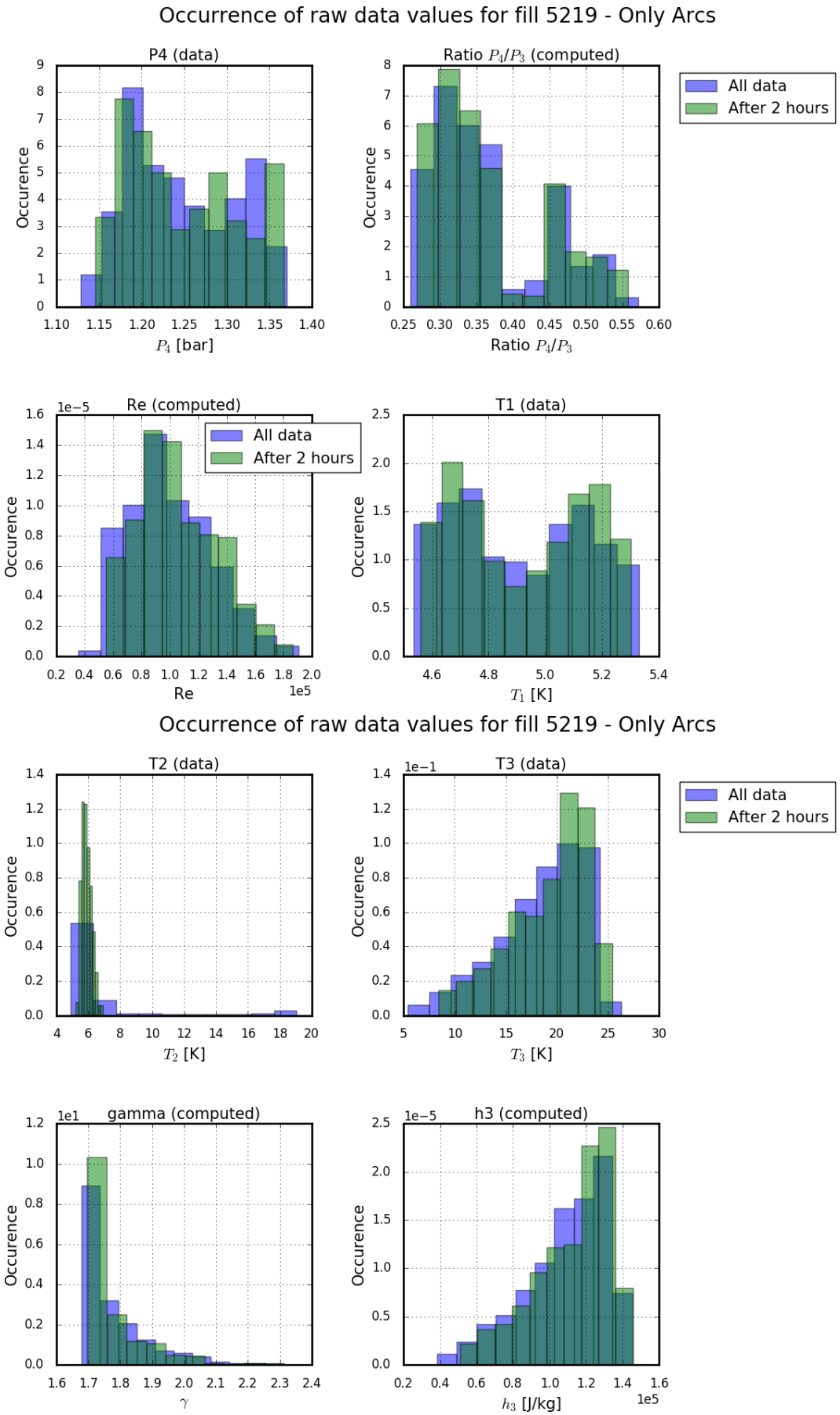

Figure 6.3: See Fig. 6.2.

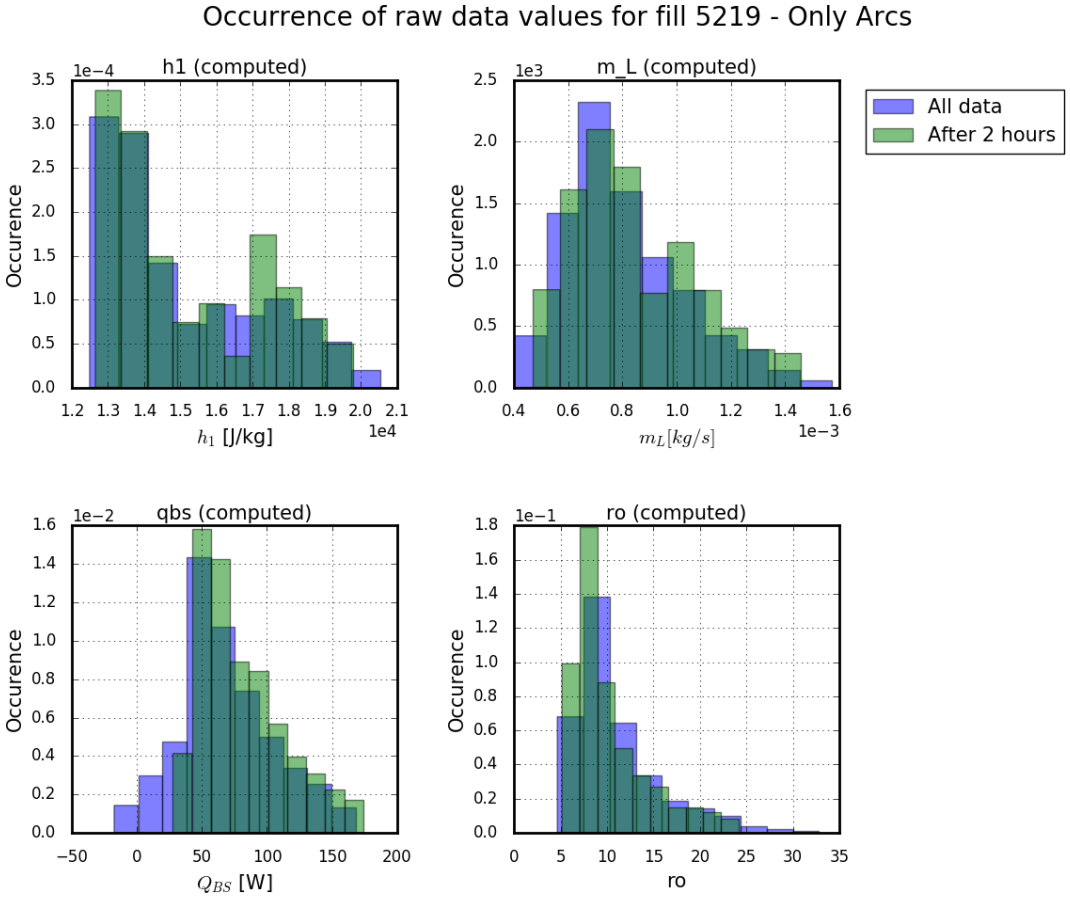

Figure 6.4: See Fig. 6.2.

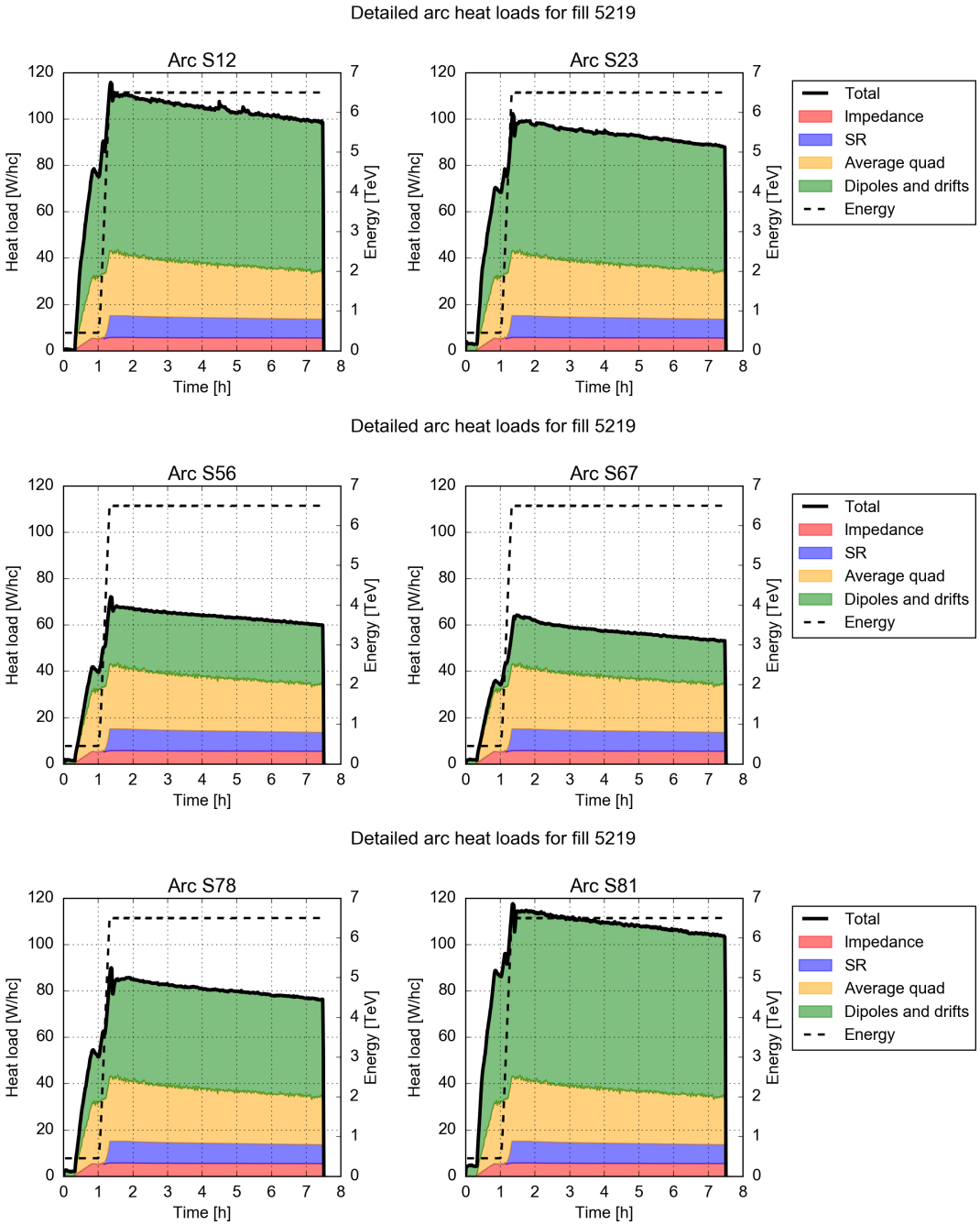

Figure 6.5: If the 3.1 m long quadrupoles in the arc cells were causing the same heat load per meter as the standalone Q6 quadrupoles, how would the measured heat loads be shared for an average cell in each arc? The corresponding plots for the remaining two arcs are given in Fig. 3.11.

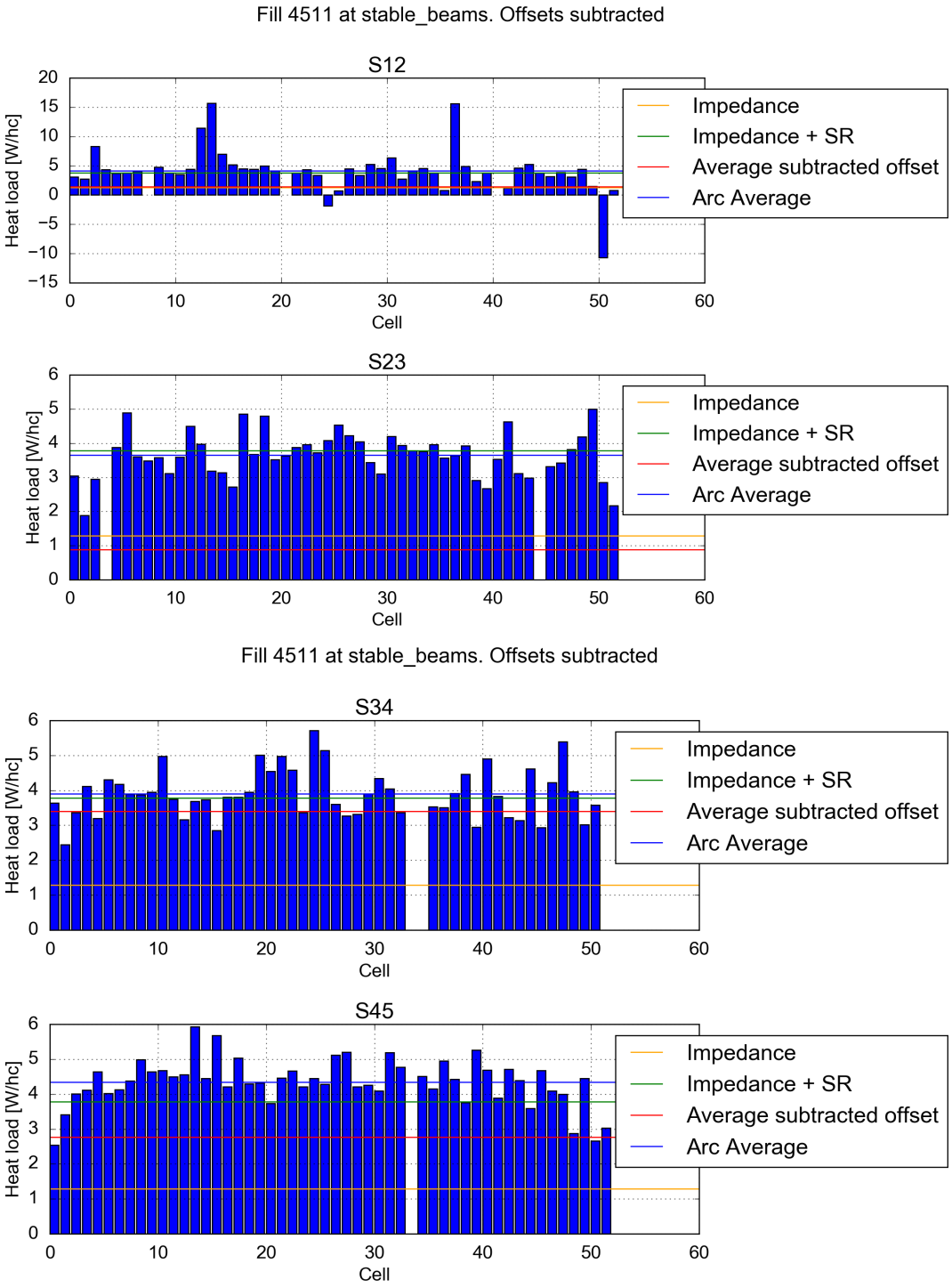

Figure 6.6: This figure corresponds to Fig. 3.15. For a fill where no substantial electron cloud effects are expected, the calculated and expected cooling powers are compared.

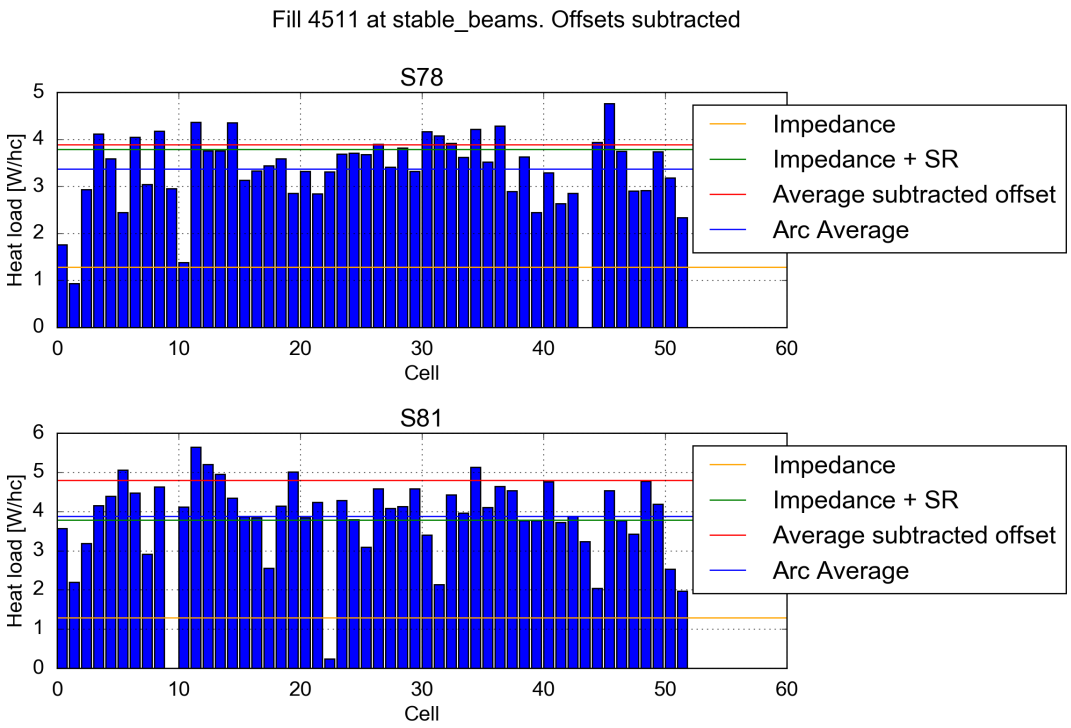

Figure 6.7: This figure corresponds to Fig. 3.15.

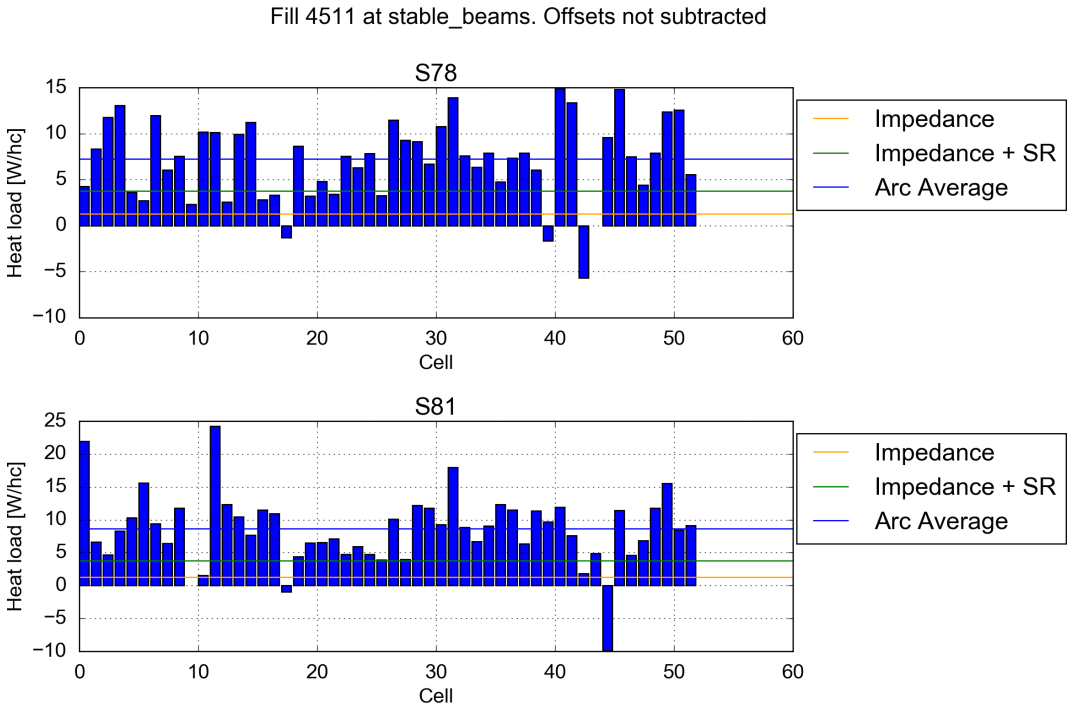

Figure 6.8: This figure corresponds to Fig. 6.7, however the offsets have not been subtracted for the individual cells. Consequently, the measured and expected cooling powers do not match to a similar extend, but differ by several Watts.

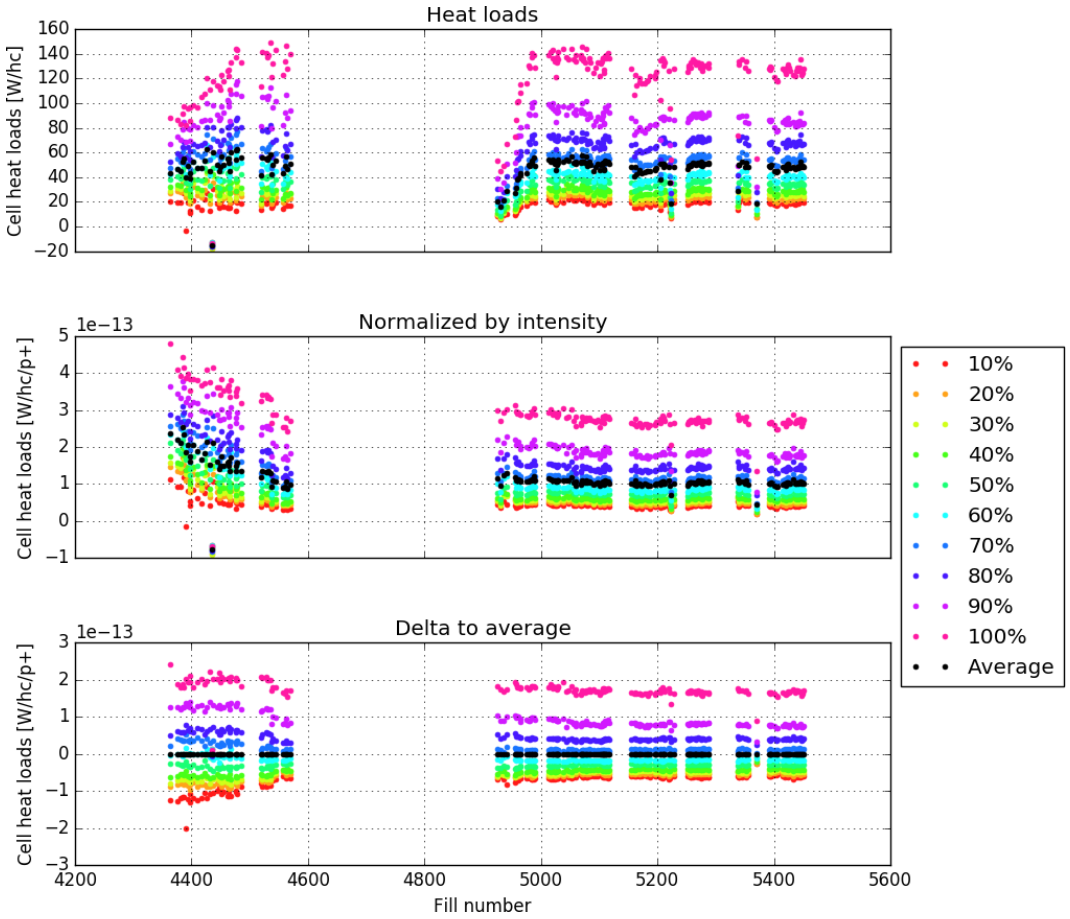

Figure 6.9: These plots show that the differences between the cells as discussed in Sec. 4.2 are already present at injection energy.

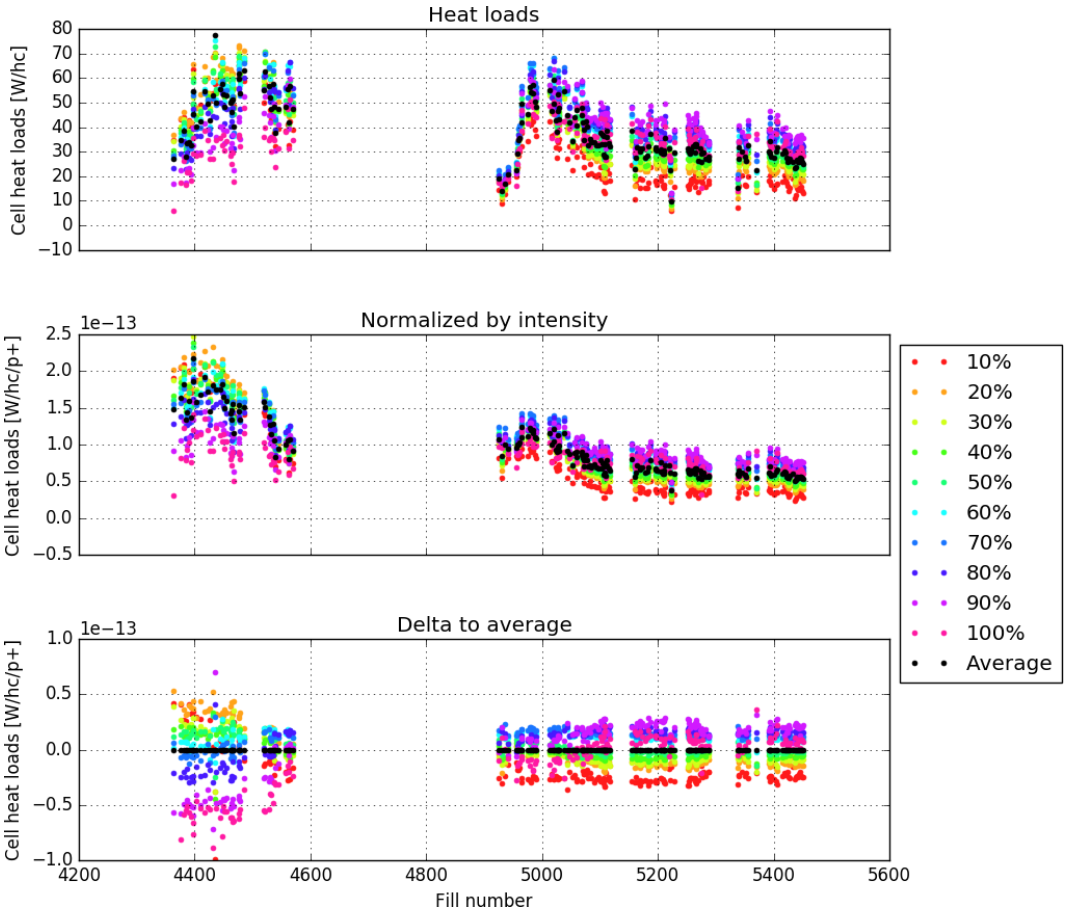

Figure 6.10: These plots show the difference in heat loads before and after the energy ramp up from 450 GeV to 6.5 TeV. The clear distinction between the groups of cells does not hold any longer.

[1] G. Aad et al., Combined Measurement of the Higgs Boson Mass in pp Collisions at $\sqrt{s} = 7$ and 8 TeV with the ATLAS and CMS Experiments, Physical Review Letters 114 (19).

[2] F. Bordry, Chamonix 2016 conclusions, presentation at Chamonix workshop 2016.

[3] CERN, Accélérateurs du CERN, `http://project-integration-accelerateurs.web.cern.ch` (figure).

[4] G. Apollinari, I. B. Alonso, O. Brüning, M. Lamont, L. Rossi, High-Luminosity Large Hadron Collider (HL-LHC), CERN, Geneva, 2015, Preliminary Design Report.

[5] G. Iadarola, Electron Cloud studies for CERN particle accelerators and simulation code development, Ph.D. thesis, University of Naples Federico II (2014).

[6] K. Ohmi, L. Mether, D. Schulte, F. Zimmermann, Study of Electron Cloud Instabilities in FCC-hh, in: Proceedings, 6th International Particle Accelerator Conference (IPAC 2015): Richmond, Virginia, USA, May 3-8, 2015, 2015.

[7] B. Henrist, N. Hilleret, M. Jiménez, C. Scheuerlein, M. Taborelli and G. Vorlaufer, Secondary electron emission data for the simulation of electron cloud, in: ECLOUD'02: Mini-workshop on electron-cloud simulations for proton and positron beams, CERN, Geneva, Switzerland, 15-18 Apr 2001: Proceedings, 2002.

[8] V. Baglin, I. Collins, B. Henrist, N. Hilleret and G. Vorlaufer, A Summary of main experimental results concerning the secondary electron emission of copper, LHC Project Report 472.

[9] R. Cimino, I. R. Collins, M. A. Furman, M. Pivi, F. Ruggiero, G. Rumolo, F. Zimmermann, Can low-energy electrons affect high-energy physics accelerators?, Phys. Rev. Lett. 93.

[10] R. Cimino, I. Collins, Vacuum chamber surface electronic properties influencing electron cloud phenomena, LHC Project Report 669.

[11] M. T. A. Kuzucan, H. Neupert, H. Störi, Secondary Electron Yield on Cryogenic Surfaces as a Function of Physisorbed Gases, in: Proceedings of the IPAC11 International Particle Accelerator Conference, San Sebastian, Spain, 2011.

[12] R. Cimino, L. A. Gonzalez, R. Larciprete, A. Di Gaspare, G. Iadarola, G. Rumolo, Detailed investigation of the low energy secondary electron yield of technical cu and its relevance for the lhc, Phys. Rev. ST Accel. Beams 18.

[13] Proceedings of the ECLOUD '12 Workshop on Electron-Cloud Effects, CERN, Geneva, 2013, comments: 39 lectures, 286 pages, published as CERN Yellow Report https://cds.cern.ch/record/1529710?ln=en.

[14] E. Hatchadourian, P. Lebrun, L. Tavian, Supercritical Helium Cooling of the LHC Beam Screens, LHC Project Report 212.

[15] E. Ödlund, Virtual Instrumentation: Introduction of virtual flow meters in the LHC cryogenics control system, Ph.D. thesis, Linköping University (2007).

[16] O. S. Brüning, P. Collier, P. Lebrun, S. Myers, R. Ostojic, J. Poole, P. Proudlock, LHC Design Report, CERN, Geneva, 2004.

[17] K. Brodzinski, L. Tavian, First Measurements of Beam-Induced Heating on the LHC Cryogenic System, Tech. Rep. CERN-ATS-2013-009, CERN, Geneva (Jan 2013).

[18] Cryodata INC, Users Guide to HEPAK, Louisville, Colorado, 1999.

[19] B. Bradu, Private message, 01.02.2017.

[20] Steven W. Van Sciver, Helium Cryogenics, 2nd Edition, Springer, New York, 2012.

[21] Wikipedia, Reynolds number, `https://en.wikipedia.org/wiki/Reynolds_number`, accessed 13.02.2017 (2017).

[22] B. Bradu, LHC Beam Screen Heat Loads, `https://indico.cern.ch/event/592369/`, presentation at Electron Cloud Meeting 36, 12.12.2016 (figure).

[23] E. Métral, Beam Screen Issues, Presentation at EuCARD - AccNet mini workshop on a "High Energy LHC" (2010).

[24] G. Iadarola, E. Metral, G. Rumolo, Beam induced heat loads on the beam-screens of the twin-bore magnets in the IRs of the HL-LHC, Tech. rep., CERN, Geneva, internal CERN note (Sep 2016).

[25] K. Wille, Physik der Teilchenbeschleuniger und Synchrotronstrahlungsquellen, 2nd Edition, Teubner, Stuttgart, 1996, English title: The Physics of Particle Accelerators: An Introduction.

[26] J. M. Jimenez, G. Arduini, P. Collier, G. Ferioli, B. Henrist, N. Hilleret, L. Jensen, K. Weiss, F. Zimmermann, Electron cloud with LHC-type beams in the SPS: A review of three years of measurements, in: ECLOUD'02: Mini-workshop on electron-cloud simulations for proton and positron beams, CERN, Geneva, Switzerland, 15-18 Apr 2001: Proceedings, 2002.

[27] G. Iadarola, P. Dijkstal, LHC Heat Loads: Observations with different bunch spacings, Presentation at HSC section meeting https://indico.cern.ch/event/612111/ 20.02.2017.

[28] B. Salvant, Beam spectrum computations, Presentation at HSC section meeting https://indico.cern.ch/event/612111/ 20.02.2017.

[29] V. Baglin, I. R. Collins, O. Gröbner, Photoelectron Yield and Photon Reflectivity from Candidate LHC Vacuum Chamber Materials with Implications to the Vacuum Chamber Design (LHC-Project-Report-206. CERN-LHC-Project-Report-206).

[30] H. Bartosik, G. Iadarola, K. Li, L. Mether, A. Romano, G. Rumolo, M. Schenk, Beam dynamics observation of the 2015 high intensity scrubbing runs at the CERN SPS, in: Proceedings of the IPAC16 International Particle Accelerator Conference, Busan, Korea, 2016.

[31] B. Bradu, Private message, 10.02.2017.